AMERICAN UNIVERSITY OF BEIRUT

CFD SIMULATION OF CREEPING FLOWS IN A NOVEL PRINTED-CIRCUIT HEAT EXCHANGER

by
TAMARA ALI AL HASSAN

A thesis
submitted in partial fulfillment of the requirements
for the degree of Master of Science
to the Baha and Walid Bassatne Department of Chemical Engineering and Advanced Energy
of the Maroun Semaan Faculty of Engineering and Architecture
at the American University of Beirut

Beirut, Lebanon
September 2019

AMERICAN UNIVERSITY OF BEIRUT

CFD SIMULATION OF CREEPING FLOWS IN A NOVEL PRINTED-CIRCUIT HEAT EXHANGER

by

TAMARA ALI AL HASSAN

Approved by:

Dr. Fouad Azizi, Associate Professor — Advisor
Department of Chemical and Petroleum Engineering

Dr. Walid Saad, Associate Professor — Member of Committee
Department of Chemical and Petroleum Engineering

Dr. Marwan Darwish, Professor — Member of Committee
Department of Mechanical Engineering

on behalf of Dr. Habchi

Dr. Charbel Habchi, Assistant Professor — Member of Committee
Department of Mechanical Engineering, Notre Dame University

Date of thesis defense: September 4, 2019

AMERICAN UNIVERSITY OF BEIRUT

THESIS, DISSERTATION, PROJECT RELEASE FORM

Student Name:

AlHassan	Tamara	Ali
Last	First	Middle

☒ Master's Thesis ○ Master's Project ○ Doctoral Dissertation

☒ I authorize the American University of Beirut to: (a) reproduce hard or electronic copies of my thesis, dissertation, or project; (b) include such copies in the archives and digital repositories of the University; and (c) make freely available such copies to third parties for research or educational purposes.

☐ I authorize the American University of Beirut, to: (a) reproduce hard or electronic copies of it; (b) include such copies in the archives and digital repositories of the University; and (c) make freely available such copies to third parties for research or educational purposes after:

One ---- year from the date of submission of my thesis, dissertation, or project.
Two ---- years from the date of submission of my thesis, dissertation, or project.
Three ---- years from the date of submission of my thesis, dissertation, or project.

T.A.H 5/9/2019

Signature Date

ACKNOWLEDGMENTS

First, I would like to thank my thesis advisor Dr. Azizi Fouad of the Chemical and Petroleum Engineering Department. I am indebted to him for his constant help and guidance throughout my research. He allowed this paper to be my personal creation, but placed me on the right track whenever the situation called for.

I would also like to thank my family who were always supporting me. This work would not have been possible without their encouragement and endless inspiration.
I would like to acknowledge every person who directly or indirectly supported and helped me in creating this paper.

AN ABSTRACT OF THE THESIS OF

Tamara Ali Al Hassan for Master of Science
Major: Chemical Engineering

Title: CFD simulation of creeping flows in a novel printed-circuit heat exchanger

Many mixing processes make use of micro-structures to enhance the blending effect of viscous fluids at low Reynolds numbers. These mixers can be either actively or passively driven. The current work focuses on split and recombine micro-mixers which can be employed as heat exchangers, reactors, simple mixers, or all of that combined. In this work, a comprehensive examination of different structures, along with a newly proposed one will be presented.

In order to highlight the performance of the proposed mixer under creeping flow conditions, the various designs were compared against each other in terms of pressure drop and mixing quality for Reynolds numbers ranging between 0.001 up to 10. For this reason, a finite element solver, Ansys Polyflow, was used to calculate the pressure drop, Fanning friction factor, concentration profile, and segregation scales. Results show that the newly proposed mixer exhibits a superior performance by means of a better mixing quality and a lower energy consumption rate.

CONTENTS

NOMENCLATURE

C_j	Concentration of material point j	[-]
$C_i^{'}$	Concentration of the first material point of an i^{th} pair	[-]
$C_i^{''}$	Concentration of the second material point of an i^{th} pair	[-]
C_{mean}	Mean concentration	[-]
CoV	Concentration coefficient of variance	[-]
C_p	Heat capacity	[J/kg.K]
D_h	Hydraulic diameter	[m]
f	Fanning friction factor	[-]
GCI	Grid convergence index	[%]
k	Thermal conductivity	[W/m.K]
L	Residence length	[m]
M	Total number of pairs of material points	[-]
N_t	Total number of material points	[-]
p	Pressure	[Pa]
R	Auto-correlation coefficient	[-]
R	Distance between two material points	[m]
Re	Reynolds number	[-]
S	Scale of segregation	[m]
$s_{concentration}$	Standard deviation of concentration at a cross-sectional area	[-]
T	Time	[s]
U_m	Mean velocity of a fluid	[m/s]

$\boldsymbol{v}$	Velocity vector	[m/s]
	Position vector	[m]

Greek Symbols

α	Volume fraction of U_m in Chen and Gray geometries	[-]
α'	Volume fraction of U_m in Double geometry	[-]
β	Volume fraction of $U_m/2$ for Chen and Gray geometries	[-]
β'	Volume fraction of $U_m/2$ for Double geometry	[-]
δ	Artificial compressibility factor	[Pa]
δ'	Volume fraction of $U_m/4$ for Double geometry	[-]
Δp	Pressure drop	[Pa]
ξ	Distance at which R = 0	[m]
ρ	Density	[$kg.m^{-3}$]
ρ'	Artificial density	[-]
σ^2	Variance of concentration	[-]
τ	Pseudo-time	[s]
μ	Viscosity	[Pa.s]

ILLUSTRATIONS

TABLES

CHAPTER I

INTRODUCTION

The overall trend in industrial processes is to achieve cleaner production, improved energy efficiency, reduced environmental impact, and the use of compact and multifunctional units when possible. These aims are the main drive for major progresses in intensifying mass and heat transfer processes. One direct example is the use of multifunctional exchangers/reactors (MERs) that rely on the coupling of fluid mechanics, heat, and mass transfer in the presence of a chemical reaction. The use of these MERs is gaining momentum in various industries, including, pharmaceutical, food processing, polymer synthesis, fine chemicals, and petrochemical industries (Anxionnaz et al., 2008; Thakur et al., 2003).

To achieve order of magnitude reduction in size, the process unit should typically operate in one of two different flow regimes, namely, turbulent or chaotic laminar flow. While turbulent flow is generally not recommended in small scale processes; and requires high energy input in the case of mixing of viscous fluids; chaotic laminar flow becomes more desirable.

Achieving a laminar chaotic behavior relies on the use of either active or passive mixers. The former type utilizes various external energy forces in order to disturb the fluids or to enlarge the contact area between them. Their driving force can be either pressure-, sound-, electricity-, heat-, or magnetic-based (Marques and Fernandes, 2011). Various configurations of such active mixers are shown in Figure 1.

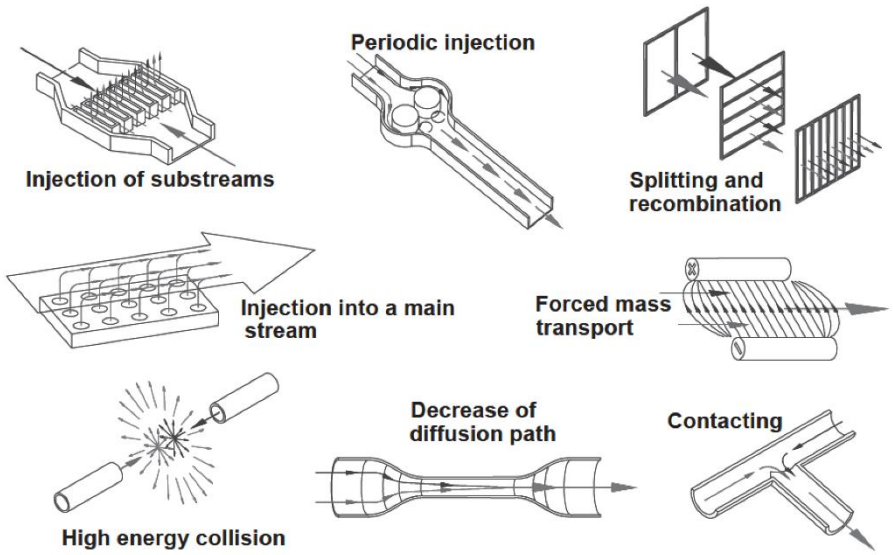

Figure 1: Selection of active and passive micromixers

On the other hand, passive mixers increase the contact area between the fluids by relying only on geometrical changes inside the mixer without the need for external forces. This can be achieved by introducing micro-structures into the channels to create chaos or by continuously applying stretching and folding processes along the length of the mixer. Such manipulations result in an enhanced mixing quality at considerably lower energy requirements.

From this perspective, split-and-recombine (SAR) configurations create chaotic advection by inducing abrupt changes in the flow direction (Ghanem et al., 2013) where the streams divide, then rotate in bends, and finally recombine. Changing the flow topology by split-and-recombine reactors (SAR), has proven successful in achieving efficient mixing particularly in low-Reynolds-number flows, and while handling viscous flows. The principle is based on baker's transformation, which relies on continuously

squeezing in the y-direction while stretching in the x-direction, then cutting in two and stacking. Therefore, a two-strip domain becomes four after one iteration. After n iterations 2n alternating strips of depth 1/2n are obtained as illustrated in Figure 2.

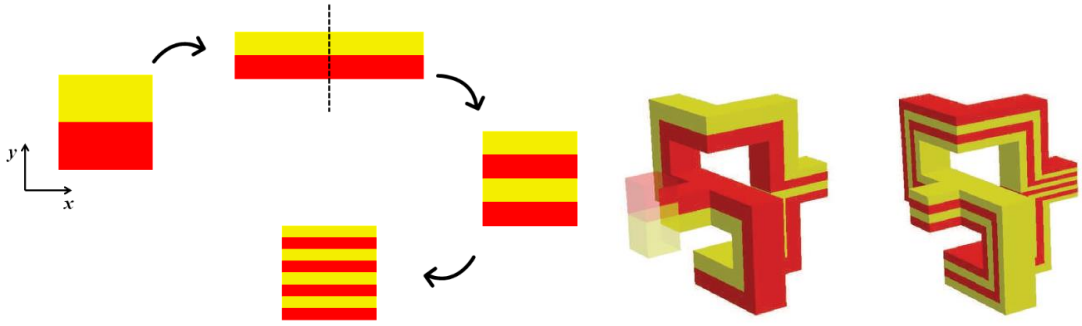

Figure 2: *Left*: Cross-section illustrating the Baker's transformation after two iterations. *Right*: Illustration of a 3D mixing pattern (Carrière, 2007) in two consecutive elements.

To further promote heat and mass transfer intensification, hence the overall efficiency for a passive mixer, the geometrical construction that influences the flow structure are modified in such a way to promote secondary transverse flows (Anxionnaz-Minvielle et al., 2017; Ghanem et al., 2013). Consequently, changing the flow topology becomes crucial to achieve efficient mixing and to handle viscous flows and the only power required is the pumping power to drive the fluids inside the channels. A search of the literature results in tens of studies conducted on split-and-recombine reactors in the past 10 years, each of which highlights the efficiency and importance of a given proposed geometry by means of experimental and/or numerical tests. A detailed description of the various geometries along with their performance will be provided in the following chapter. However, the design of these SAR mixers plays a

crucial role in determining their efficiency since it is directly linked to controlling the flow hydrodynamics. The goal is therefore to develop a SAR mixer (or SAR-MER) that is efficient enough to be competitive with other already existing configurations, sufficiently compact and multifunctional to reduce its capital cost, and simple to manufacture to allow its industrial development.

Recently, Habchi et al. (Habchi et al., 2018) studied the mixing of inviscid fluids under laminar conditions in a novel type of SAR topology. This MER was called the "Double SAR" and is characterized by double separation and recombination in order to increase the lateral gradients and destroy the concentration profile faster.

The aim of the current work is therefore to numerically evaluate the performance of the "Double SAR" in terms of mixing efficiency and energy consumption under creeping flow conditions using viscous fluids. Its performance will also be compared with other commonly used geometries in order to better quantify the mixing enhancement and power requirements. This will be achieved using a commercial CFD software, ANSYS Polyflow, in order to compute several mixing indices and quantify the pressure drop and friction factors along the mixers.

This thesis will be divided into several chapters. In the second chapter, a literature review about passive SAR micro-mixers is presented. The third chapter includes the approach of running the CFD simulations: the relevant definitions and equations are listed, followed by a description of the numerical simulations. The fifth chapter will present the results to assess the performance of the proposed geometry and

compare it with the other configurations. Finally, the conclusions and recommendations will be highlighted in the final chapter.

CHAPTER II

LITERATURE REVIEW

A search of the literature results in tens of studies conducted on split-and-recombine reactors in the past 10 years, each of which highlights the efficiency and importance of a given proposed geometry by means of experimental and/or numerical tests. Therefore, this section presents a brief review of the various studies that can be found in the literature while presenting their main findings and conclusions.

Aubin et al. (2003), numerically investigated the mixing performance of two SAR geometries, namely, the “herringbone” and “diagonal” mixers in the laminar flow regime corresponding to Re = 2 (Figure 3). They studied the dispersion of particles using CFD simulations and employed macro-scale quantitative analysis methods that are traditionally used for static mixers. They concluded that the “herringbone” geometry renders very good mixing compared to the other one where very little convective mixing was observed.

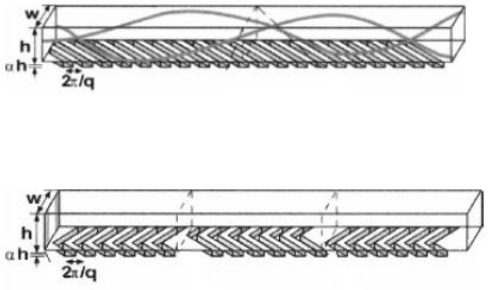

Figure 3: Schematic representation of the “herringbone” (top) and “diagonal” (bottom) mixers

They also found that methods based on variance calculations and stretching rates are more suitable for quantifying mixing than those relying on deformation rates.

Schönfeld et al. (2004), employed CFD to assess the mixing in an enhanced version of a commercial SAR mixer, namely the "caterpillar" mixer (Figure 4a). They performed CFD simulations in the laminar regime particularly at Re < 15 which rendered an almost ideal multi-lamination prediction. This was further validated experimentally by studying the mixing of water-glycerol solutions which led them to the conclusion that the mixer is suited for mixing highly viscous fluids.

Chen and Meiners (2004), suggested a design characterized by opposite chiralities to split, rotate, and recombine the fluid streams (Figure 4b). It creates a series of Baker's transformations over the fluid concentration to produce better mixing. Experimental tests at Re = 0.1 were performed to quantify the mixing performance of the proposed design. At first, efficient mixing was obtained after three stages of 1.2 mm length as diffusion was dominating at the interfaces. Then, for a higher viscosity and flowrate, a well-mixed state was achieved after five stages only, having the effects of diffusion eliminated. Additional tests at Re ranging between 0.1 and 2 were done using fluorescent dyes. The results confirmed that mixing efficiency is exponentially increased as the fluid travels inside the channels. Additionally, the geometry presented efficient mixing for short length scales even at the lowest Reynolds numbers.

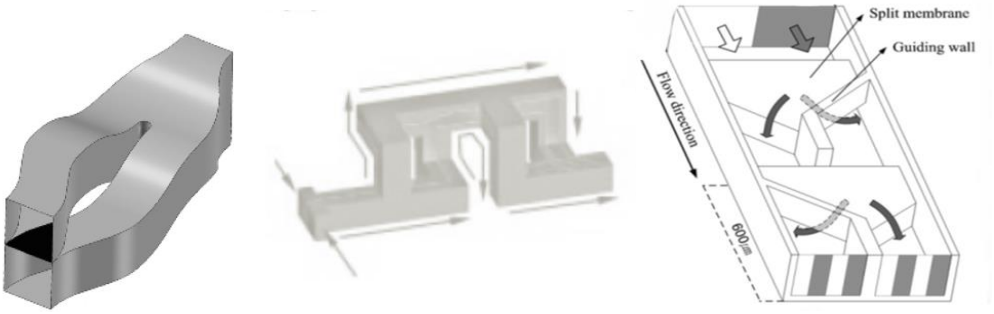

(a) Caterpillar micromixer (b) Chen SAR micromixer (c) Split micromixer

Figure 4: Elementary units of the mixers proposed by (a) Schonfeld et al. (2014), (b) Chen and Meiners (2004), and (c) Lee et al. (2006)

Lee et al. (2006) presented a new SAR design along with its manufacturing process (Figure 4c). Their design was developed to be compatible with lab-on-a-chip technologies. They tested the performance of their mixer by means of both experimental and numerical tests in the range of $0.012 < Re < 120$. They found that the number of mixing elements required to perform good mixing increases with Re based on a colorization mixing experiment of a blue dye with water, and their numerical predictions agreed well with the experiments. Their pressure drop estimation was performed numerically, and they found a linear relationship between Δp and Re.

Ohkawa et al. (2008), proposed another geometry that performs splitting and inverse recombination that is characterized by σ-shaped elements/ducts illustrated in Figure 5a. Experimental characterization of the flow and mixing efficiency were conducted by means of a decolorization reaction whereas CFD simulations were performed to check the velocity profiles as well as calculating the pressure drop. Their major finding was that for $Re< 10$, the number of mixing elements required to attain

complete mixing increased with Re whereas the simulated friction factor decreased at a rate of Re^{-1}. For Re>10 the authors observed the generation of secondary flows due to the multi-dimensionality of the mixer geometry. Moreover, they reported that the number of elements required for complete mixing is maximum in the range 10<Re<20, which subsequently decreases at Re>20. In addition, the friction factor variation with Re changes as Re gets larger than 10.

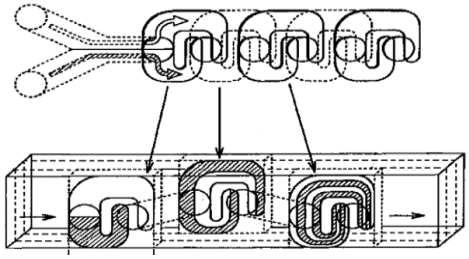

(a) σ-type plate static mixer

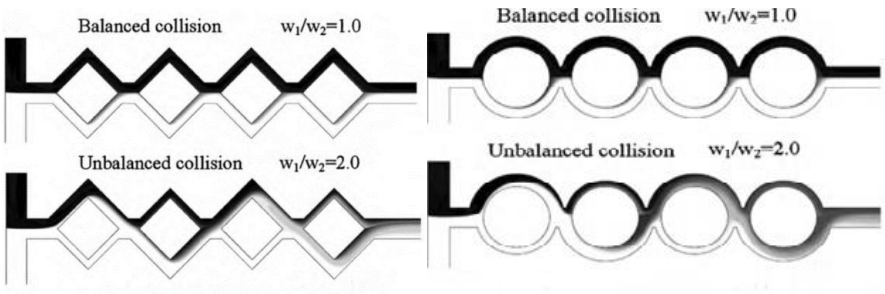

(b) Rhombic and circular sub-channels for balanced and unbalanced collisions models

Figure 5: Elements of the mixers proposed by (a) Ohkawa et al. (2008) and (b) Ansari and Kim (2010)

Ansari and Kim (2010), numerically studied the mixing performance of planar split and recombine micromixers characterized by having circular or rhombic split channels. Furthermore, these mixers have asymmetric sub-channels the width of which

was kept unequal to drive the streams to have unbalanced collisions as shown in Figure 5b.

Using a water-ethanol mixture at Re ranging between 1 and 80, the rhombic design was found to yield better mixing if the ratio between the large and small sub-channels was maintained between 3 and 4. However, mixing was always worst when the channels had the same width, regardless of their design.

Neerincx et al. (2011), proposed a new compact mixer that is characterized by its capability of splitting and recombining the flow into 24 layers in the first pass which increases to 288 after the second. It is based on a fan-shaped circular design in order to maintain a uniform distribution of flow lengths (Figure 6). The authors also found that the mixer consumes less pressure drop while providing very good mixing when compared to the Kenics static mixer and a commercially available serpentine mixer.

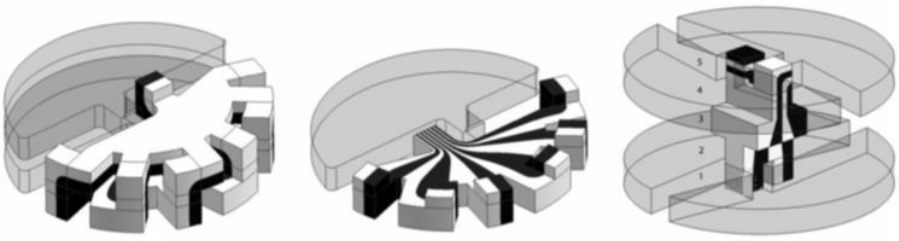

Figure 6: Different perspectives of the mixer proposed by Neerincx et al., (2011)

Chen et al. (2011a), evaluated both numerically and experimentally the performance of a new crosswise ridge mixer in the range $0.5 < Re < 50$. Their goal was to obtain physical insights of the flow characteristics and evaluate the mixing performance in such mixers. demonstrated in Figure 7a.

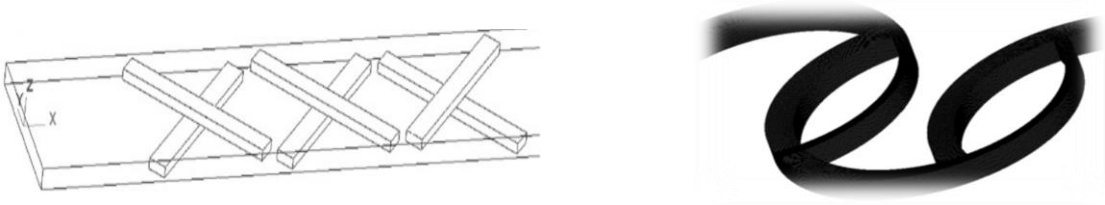

(a) Crosswise ridge micro-mixer (b) Staggered Dean Vortex mixer

Figure 7: Elements of the geometries proposed by (a) Chen et al. (2011a) and (b) Sheu et al. (2011b)

Their experiments showed that the mixing index always increased with Re and that the design characterized by slanted ridges on the bottom and top of the channels renders excellent mixing efficiency. The authors also reported that their numerical results overpredicted the experimental findings but always showed similar trends. They attributed this discrepancy to numerical diffusion.

Sheu et al. (2011b), attempted to take advantage of secondary flows (i.e. Dean's vortices) to enhance mixing in a new mixer characterized by staggered, curved, channels as shown in Figure 7b. Numerical simulations of concentration distribution and particle trajectories were used to assess the flow characteristics inside four different variants of this mixer. Their findings show that the design that resulted with the best mixing efficiency required the highest pressure drop to drive the flow. Furthermore, they noted that Dean vortices (i.e. secondary flows) were negligible for $Re < 5$ and that the mixing length required to achieve good mixing decreased with an increase in Re.

Parsa and Hormozi (2014), proposed a design based on sinusoidal walls with a T-shaped entrance presented in Figure 8a. The performance of this mixer was investigated numerically using finite element CFD codes under various design and

operating conditions. Their work focused on the hydrodynamic range of $0.2 < Re < 75$, and studied the effect of varying the phase shift, and the wavelength to amplitude ratios on the pressure drop as well as the mixing index. Optimal values for phase shift angle (between $\pi/2$ and $3\pi/4$) and wavelength were found to ensure the highest mixing efficiency and the lowest energy consumption. Their findings also highlighted that molecular diffusion is dominant for $Re < 20$, however, at $Re > 20$ secondary flows such as Dean and expansion vortices become prevalent and considerably enhance the mixing quality. Further, their numerical findings reasonably matched the experimental results.

In an attempt to reach an optimal design of 3D serpentine mixers, Hossain and Kim (2015) attempted to combine SAR patterns with serpentine design. The latter design attempts to enhance mixing by creating strong transverse flows. Using the previously proposed serpentine mixer of Ansari and Kim (2009), they introduced SAR patterns by using "OH"-shaped segments as Figure 8b. shows. The flow characteristics as well as the mixing performance were then numerically analyzed, and the results were qualitatively compared to the experimental results of Ansari and Kim (2009). Their study was performed in the Re range of 0.1 to 120 using water and ethanol as their working fluids. The introduction of the SAR patterns into the design was found to enhance mixing in the Re range of 0.1-70, with the enhancement being more pronounced in the range of 10-35.

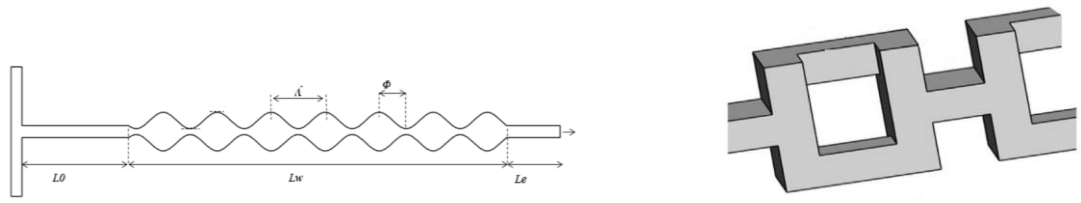

(a) Micromixer with sinusoidal walls and T-entrance (b) OH pattern of the mixer

Figure 8: Patterns of the micromixers proposed by (a) Parsa and Hormozi, (2014) and (b) Hossain and Kim, (2015)

Viktorov et al. (2015) also proposed a new geometry and investigated its performance numerically while simultaneously comparing it to two other SAR mixers. Their C-H mixer was compared to a Chain and another Teardrop mixer by means of mixing efficiency and pressure drop requirements (Figure 9). The study was conducted in the Reynolds number range between 1 and 100. Their results showed an excellent mixing efficiency for their proposed C-H mixer as compared to the other two while simultaneously exhibiting lower pressure drop requirements. However, their design showed dependency on the inlet flow ratios, especially at higher Re values.

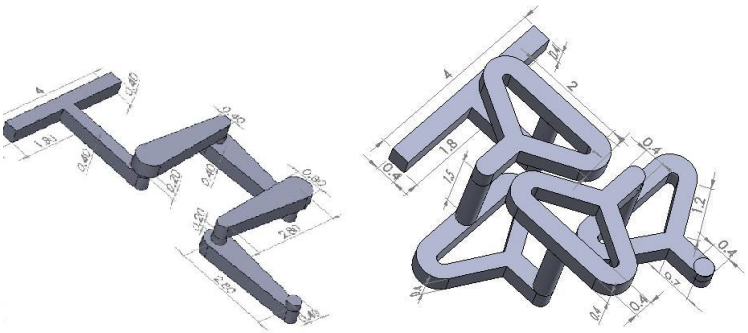

(a) Chain mixer (b) Teardrop mixer

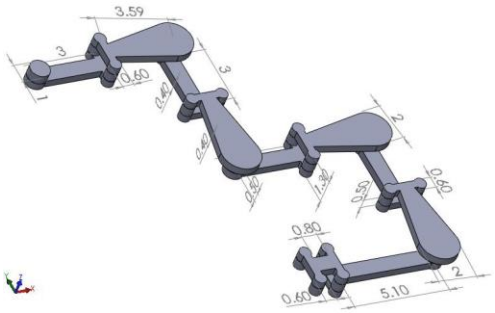

(c) C-H mixer

Figure 9: Chain, Teardrop and C-H micromixers

In two different studies, Ghanem et al. (2013a and 2013b) compared the performance of two commonly used SAR mixers, namely, the designs proposed by Chen and Meiners (2004) and Gray et al. (1999) shown in Figure 10. One of the studies considered the low Re regime ($10^{-4} < Re < 10$) (Ghanem et al., 2013b) and was focused on comparing the heat transfer capabilities of the SAR mixer, while the second looked at the transitionary region with $40 < Re < 5{,}000$ and focused on the mixing and mass transfer performance (Ghanem et al. 2013a). Mixing efficiency was quantified by studying the evolution of the iodide-iodate reaction system using a chemical probe method. In this study, the Gray mixer was found to have a superior performance compared to that of Chen and Meiners and that mixing is most efficient in the laminar regime. However, the low Re study (Ghanem et al., 2013b) was only a numerical investigation, but, in contrast to the results of the earlier study, the geometry proposed by Chen and Meiners was found to promote heat transfer more efficiently than that of Gray et al.

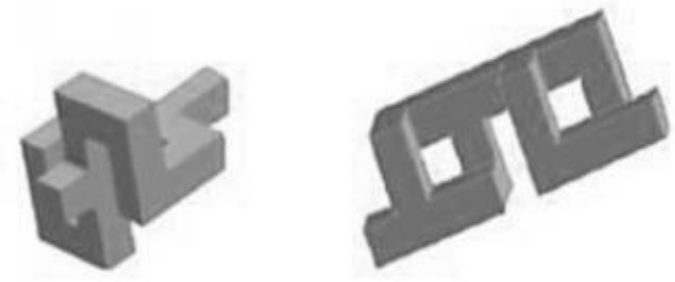

Figure 10: Elementary units of the Gray and Chen micromixers

This work was followed by a similar attempt by Jarrahi et al. (2016) who performed heat transfer experiments using these two geometries for the Re range of 100 to 3,000. However, in contrast to the work of Ghanem et al. (2013a, 2013b) who used square cross sections of 3 mm of size, Jarrahi et al. (2016) utilized circular ducts of 5 mm diameter along with 90° elbows. Their findings highlighted that the value of the convective heat transfer coefficient did not show fluctuations in the geometry of Chen and Meiners as compared to that of Gray et al. Furthermore, the design of Gray et al. was found more superior. This is because it accomplished a better heat exchange efficiency measured by the uniformity of the temperature field at the outlet of the mixer/heat-exchanger, in addition to a lower Δp over the complete range of Re.

In another attempt to study the extent of intensification the introduction of SAR patterns would have in a heat-exchanger/reactor device, Anxionnaz-Minvielle et al. (2017) experimentally tested the mixer designs of Gray et al. and Chen and Meiners. They also studied the effect of a small modification on the Gray design while comparing their results to a regular 2-D corrugated channel. Their experimental study considered the effect of changing the operating conditions on the pressure drop, heat transfer, as

well as the performance of a chemical reaction. The latter would also serve as an indication of the mixing performance. Their findings clearly highlighted the importance of SAR patterns especially when the fluids are viscous. Much higher heat transfer rates were measured in addition to an intensification of the chemical reaction as compared to the corrugated sheets at relatively lower energy consumption.

Habchi et al. (2019), also numerically investigated the Gray et al. and Chen and Meiners mixers for their dispersive and distributive mixing performance under creeping flow conditions (at Re = 0.001) using a finite volume method. The aim of their study was to prove the efficiency of SAR patterns in promoting mixing using viscous fluids. They found that the Chen and Meiners design outperformed that of Gray et al. at relatively lower energy requirements.

In summary, numerous designs and studies on split-and-recombine mixers can be found in the open literature with most of them dealing with the hydrodynamic characterization and/or the assessment of their mixing performance. Regardless of the design, there is a widespread agreement that the introduction of SAR patterns enhances mixing and that Dean vortices were always observed under laminar flow conditions (i.e. Re > 5, depending on the mixer geometry) and absent in creeping flow situations.

CHAPTER III

METHODOLOGY

As previously mentioned, various SAR geometries have been proposed to enhance mixing and heat transfer in compact units. Habchi et al. (Habchi et al., 2018) proposed a new variant that proved to be promising. This mixer is characterized by double separation and recombination in order to increase the lateral gradients and destroy the concentration profile faster. To meet the research objectives of the current work, this newly proposed geometry, the "Double SAR" will be numerically assessed and its performance compared to other commonly used geometries under creeping flow conditions. For this reason, a CFD solver based on the finite element method, ANSYS Polyflow® will be used to simulate the flow, and characterize its hydrodynamic and mixing performance in various mixers.

A. Computational Domain

All the geometries that will be investigated are formed of squared channels with a cross sectional area of 3×3 mm^2 and a hydraulic diameter of 3 mm. They are composed of multiple repetitive mixing elements. Each element is made up of channels that split the flow into several branches then recombines it to create laminations, the role of which is to increase the contact between the fluid elements and destroy the concentration profile. The complete mixer geometry is then made up of different numbers of alternating elements, and the number is chosen in fashion that conserves the residence length in all the geometries. This is shown in Table 1 which lists the number

of mixing elements for each geometry, in addition to its corresponding residence length, volume, and straight length.

Table 1: Geometrical characteristics of the full geometries

Geometry Type	Straight Duct	Chen	Gray	Double
Number of mixing elements	1	9	12	4
Hydraulic Diameter, (mm)	3	3	3	3
Residence length, (mm)	654	627	654	630
Straight length, (mm)	654	249	186	114
Volume, (mm^3)	1,450	675	540	1,458

For each mixing element, both Gray and Chen geometries, have one splitting and one recombination junction. However, the Double-SAR is characterized by the presence of a second branching where two successive splitting and recombination junctions can be found in each element. Figure 11 shows the geometry of one mixing element of the Chen (Chen and Meiners, 2004), Gray (Gray et al., 1999), Double (Habchi et al., 2018) in addition to a straight pipe. The latter was chosen to account for the role of SAR patterns on mixing enhancement in addition to its role in providing a baseline for numerical diffusion.

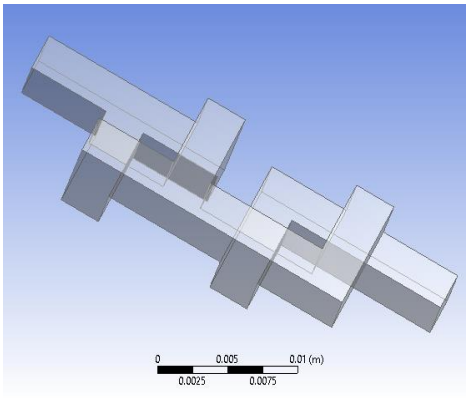

(a) Chen geometry

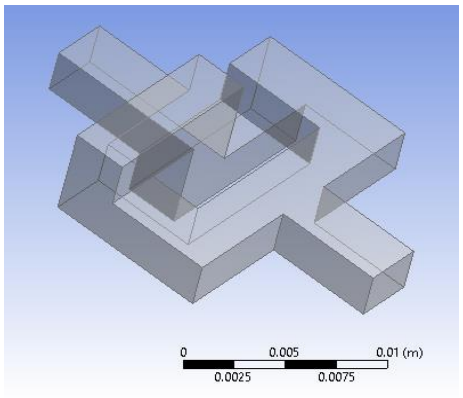

(b) Gray geometry

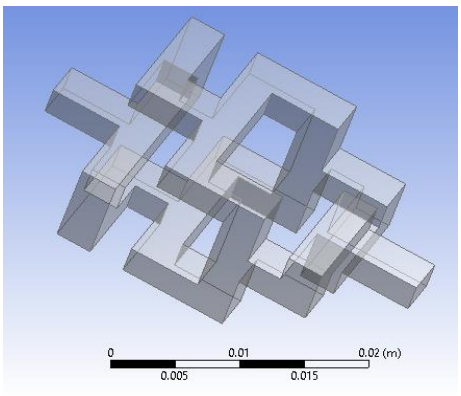

(c) Double geometry

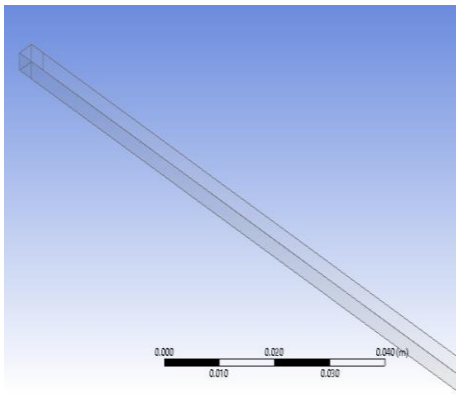

(d) Straight pipe geometry

Figure 11: One representative element of each geometry

The geometric discretization of the domains represented in Figure 11 is based on the subdivision of the geometries into discrete finite elements that result in a mesh where conservation equations can be solved (Moukalled et al., 2015). This is usually achieved in a variety of techniques leading to different types of meshes that depend on the element shape, the structure, the orthogonality, etc. For this case, a structured grid based on hexahedral elements is used to model the geometries. An illustration of the chosen mesh is presented in Figure 12 for the Double geometry.

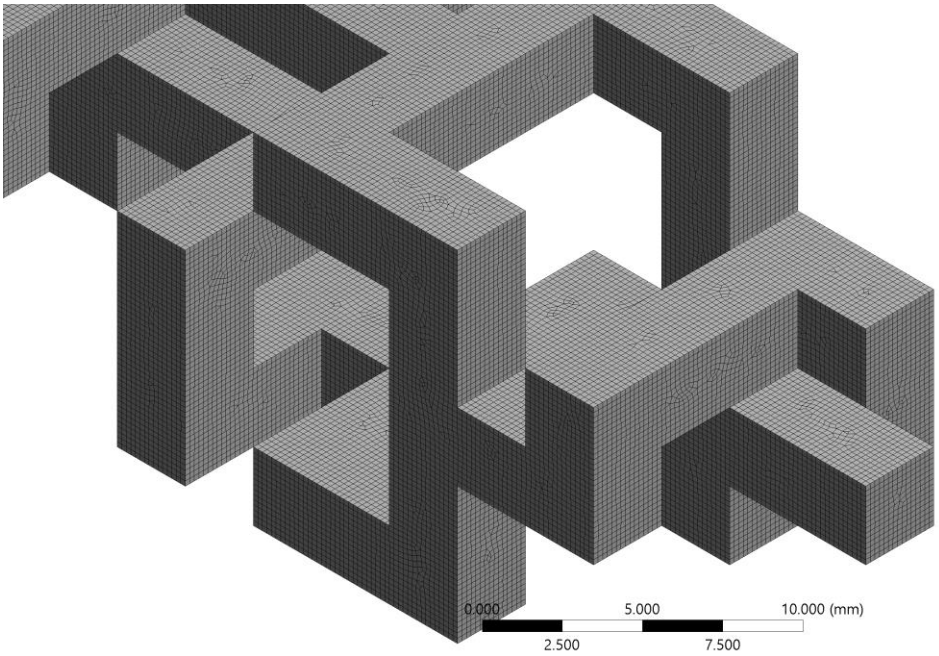

Figure 12: Illustration of the structured mesh used for the Double geometry

B. Boundary conditions and Solution method

In the current work, a 90% wt. glycerol-water solution was used for all the simulations. It was considered as a Newtonian single-phase (i.e. perfect mixing between glycerol and water). Its physical properties are listed in Table 2:

Table 2: Properties for a 90% wt. glycerol-water solution

Density, ρ (kg/m^3)	1,015
Viscosity, μ (Pa·s)	0.21
Heat Capacity, C_p (J/kg·K)	1,000
Thermal conductivity, k (W/m·K)	1.00×10^{-6}

Thermal diffusivity, α (m^2/s)	9.9×10^{-13}

In the current work, the flow was assumed Newtonian and incompressible, flowing under steady state conditions. In addition, the body and gravity forces were neglected. Based on those assumptions, the mass and momentum conservation equations governing the fluid flow are listed as follows:

$$\nabla . \boldsymbol{v} = 0 \tag{1}$$

$$\rho \boldsymbol{v} . (\nabla \boldsymbol{v}) = -\nabla p + \mu \nabla^2 \boldsymbol{v} \tag{2}$$

where, $\boldsymbol{v}$ = velocity vector, (m/s)

p = pressure (Pa);

μ = dynamic viscosity of the fluid, (Pa.s);

ρ = density of the fluid (kg/m^3);

ANSYS Polyflow uses a finite-element method to simulate flow applications. Such problems require specific interpolation schemes for the velocity and the pressure to solve continuity and momentum equations.

When the divergence of velocity is required to vanish in the mass conservation equation, the pressure term in the momentum equation becomes bounded by the satisfaction of the constraint imposed on the velocity field. Hence, the pressure term is forced to adjust itself instantly to satisfy the divergence-free condition (Donea and Huerta, 2003).

In order to satisfy this incompressibility constraint, Polyflow uses a mixed finite-element method which imposes some limitations on the choice of interpolation schemes for velocity and pressure. (ANSYS® Inc., 2017). In fact, the selected interpolation schemes are polynomials that approximate the value of flow variables at each element (Heniche and Tangu, 2008). Those schemes must satisfy the condition known as the LBB (Ladyzhenskaya–Babuška–Brezzi) criterion (Langtangen et al., 2002). It is defined as a tool that determines the compatibility between pressure and velocity interpolation functions to ensure a solvable system and a convergent, stable method.

In the present work, a multifrontal direct solver is adopted using a "linear velocity-constant pressure" interpolation scheme and a convergence criterion of 10^{-6}. The linear representation of the velocity along with constant pressure at each element offer a low computational cost with good accuracy in the 3-D domains, but may lead to instabilities in the pressure term as this formulation violates the LBB criterion. Consequently, oscillations in the pressure field occur leading to inaccurate results.

In this case, an artificial compressibility term is added to the continuity equation (Chorin, 1997). This method aims at transforming the elliptic incompressible differential equation into a hyperbolic compressible model by introducing an artificial term to the equation as shown in Equation (3):

$$\frac{\partial \rho'}{\partial \tau} + \nabla . \boldsymbol{v} = 0 \tag{3}$$

where, $\boldsymbol{v}$ = velocity vector, (m/s);

ρ' = artificial density;

τ = auxiliary variable, denoted as pseudo-time, (s);

The artificial density is related to pressure by the artificial equation of state defined as:

$$p = \rho' \times \delta \tag{4}$$

where, δ = artificial compressibility factor, (Pa);

Hence, the artificial continuity equation becomes:

$$\frac{1}{\delta}\frac{\partial p}{\partial \tau} + \nabla . \boldsymbol{v} = 0 \tag{5}$$

And the momentum equation also becomes:

$$\frac{\partial \boldsymbol{v}}{\partial \tau} + \rho \boldsymbol{v} . (\nabla \boldsymbol{v}) = -\nabla p + \mu \nabla^2 \boldsymbol{v} \tag{6}$$

This system of equations becomes solvable and leads to a stable solution for the linear velocity- constant pressure interpolation schemes. As τ approaches infinity, the solution of the non-steady state equations (5) and (6) asymptotically tends to the solution of the steady-state equations (1) and (2). The solution then becomes independent of τ and δ since it behaves similarly to a relaxation factor.

To solve this new system of governing equations, the following boundary conditions were imposed:

- **Normal velocity at the inlet for a constant velocity profile.**

- **Outflow condition at the outlets.**
- **No slip condition at the walls.**
- **Steady-state simulations**

After computing the velocity and pressure equations, the parameters of interest would then be evaluated.

To complete the mixing studies, a concentration profile that is characterized by two equal horizontal planes of 1,000 material points with scalar concentrations of 0 and 1 was imposed at the inlet , as shown in Figure 13.

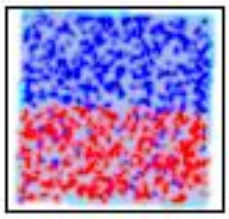

Figure 13: Concentration profile at the inlet

The values obtained from the computation of the velocity are then used to calculate the particles trajectories inside the flow field. The successive positions of the material points are evaluated by integrating the equation of motion for each particle:

$$\frac{d\boldsymbol{X}}{dt} = \boldsymbol{v} \tag{7}$$

where, $\boldsymbol{X}$ = position vector, (m);

t = time (s);

Polyflow uses an explicit fourth order Runge-Kutta scheme for the integration of the equation of motion. Firstly, the finite element containing the material point is identified. Then, the integration is performed over that element until its border is reached. Next, the following element is identified and the integration is carried on. An integration time step per element is specified as 3 steps per element for the calculations. The tracking of particles would then allow the determination of the variation in the mixing intensity from the inlet to the outlet of the micromixers.

1. Flow Regime

In the present study, the flow falls in the creeping flow regime or what is also known as the "Stokes flow". These flows are characterized by the dominance of viscous forces over advective inertial forces. Creeping flows take place under very slow velocities, highly viscous fluids or small length-scales of mixing paths. Accordingly, this flow regime is described at low range of Reynolds numbers, always smaller than unity (i.e. Re < 1). In the current case, the corresponding Reynolds number is defined based on the hydraulic diameter of the channel according to the following equation,

$$Re = \frac{\rho U_m D_h}{\mu}$$

where, ρ = density of the fluid (kg/m^3);

μ = dynamic viscosity of the fluid, (Pa.s);

U_m = mean velocity of the fluid, (m/s);

D_h = hydraulic diameter of the flow channel, (m);

In the current study, Re numbers were pre-selected for all simulations in the four geometries. These values were set at 0.001, 0.01, 0.1, 1, and 10. It should be noted that while the latter value of Re falls outside the creeping flow regime, it was selected to have an over-lap region with other studies being conducted in the laminar regime (Re > 1) using a finite volume solver. Such overlap would allow further validation of the results.

C. Hydrodynamic Characterization of the Flow

1. Pressure Drop

The economic viability of any process unit is partly determined by its operating cost which, in turn, is largely influenced by its energy consumption. Therefore, knowledge of the pressure drop across the mixer is an important factor in order to determine its industrial acceptance. In general, SAR micormixers are characterized by their low energy consumption which mainly originates from the pumping power required to drive the flow.

Pressure drop is produced either from viscous and wall friction losses or from local flow losses inside the geometry. In the laminar regime, pressure drop is directly proportional to the square of the mean velocity inside the mixer. For a straight duct, it is calculated as follows:

$$\Delta p = 2f \frac{\rho \, L \, {U_m}^2}{D_h} \tag{8}$$

where, f = pipe Fanning friction coefficient;

L = residence length, (m);

ρ = density of the fluid, (kg/m^3);

U_m = mean velocity, (m/s);

D_h = hydraulic diameter, (m);

For SAR geometries, the flowrate is split inside the channels. This affects the calculation of the pressure drop as different mean velocities occur inside the micromixer. In the cases of the Gray and Chen geometries, the mean velocity varies between U_m and $U_m/2$ having only one SAR pattern per mixing element. As for the Double-SAR, the mean velocity can be reduced to $U_m/4$ in certain channels due to the presence of two SAR patterns per mixing element. Based on that, the mean velocity and the residence length for which this velocity occurs differ from one geometry to the other and the pressure drop equation becomes:

$$\Delta p = 2f \frac{\rho \sum_{i=0}^{2} L_i \, {U_i}^2}{D_h} \tag{9}$$

Where "i" is an index referring to the velocity occurring inside the channel. For instance, a value of i = 0 designates the occurrence of the velocity U_m, while values of i = 1 and i = 2 designate the occurrence of $U_m/2$ and $U_m/4$ respectively.

2. Fanning Friction Factor

SAR structures rely on flow splitting inside the unit. Consequently, the velocity will not remain constant throughout all the channels. This leads to a lower pressure drop. In order to account for the effect of such velocity variations, the Fanning friction

factor can be used as another measure of energy consumption. This parameter is computed as:

$$f = \frac{\Delta p \, D_h}{2L\rho {U_m}^2} \tag{10}$$

The theoretical Fanning friction factor for a squared straight channel is given in Equation (11) (Ohkawa et al., 2008).

$$f = \frac{14.227}{Re} \tag{11}$$

For SAR mixers, the velocity reduction should be taken into account. Following the approach of Habchi et al. (2019), to quantify friction in each geometry, the friction factor should be calculated as the sum of the friction factors in the various channels where the flow velocity varies.

In the case of the Gray et al. and Chen and Meiners geometries, the velocity is split into two. This is determined by the inherent geometry of the mixer. However, in the "Double SAR" geometry, the velocity is further divided by an additional factor of two. This means the average flow velocity in the various channels might assume a value of U_m or $U_m/2$ or $U_m/4$, depending on the location. According to Habchi et al. (2019), the equation of the friction factor for the Gray et al. and Chen and Meiners geometries can be written as:

$$f = \alpha \frac{\Delta p \, D_h}{2L\rho {U_m}^2} + \beta \frac{\Delta p \, D_h}{2L\rho (\frac{U_m}{2})^2} \tag{12}$$

where, α = fraction of volume corresponding to U_m;

β = fraction of volume corresponding to $U_m/2 = 1-\alpha$;

Similarly, for the Double geometry, α' and β' represent the fractions of volume corresponding to U_m and $U_m/2$. An additional parameter designated by δ' is introduced, representing the fraction of volume corresponding to $U_m/4$. It has a value equivalent to $\delta' = 1-\alpha'-\beta'$. Accordingly, a new term that takes into account the new velocity $U_m/4$, the corresponding length, and the fraction of volume for which $U_m/4$ occurs is added to equation of the friction factor. The equation becomes:

$$f = \alpha' \frac{\Delta p \, D_h}{2L\rho {U_m}^2} + \beta' \frac{\Delta p \, D_h}{2L\rho (\frac{U_m}{2})^2} + \delta' \frac{\Delta p \, D_h}{2L\rho (\frac{U_m}{4})^2} \quad (13)$$

The evaluation of the friction factor in the case of SAR structures offers a better understanding of energy consumption as it takes into account the effect of splitting the velocities as shown in the above equations. The smaller velocities occurring due to flowrate division may reduce pressure drop inside the mixer. However, this would not be enough to characterize the mixer itself in terms of friction losses. The friction factor arises in such case to assess the geometry in terms of energy consumption while scaling out the velocity issue.

D. Mixing Characterization

Mixing quantification has been the subject of various investigations and debate in the open literature. Kukukova et al. (2009) reported the presence of a multitude of definitions for mixing without any one of them clearly describing the full range of

problems in the industry. For this reason, Kukukova et al. (2009), presented an alternate approach, in which they defined segregation over three different dimensions, namely, intensity of segregation (concentration scale), scale of segregation (length scale), and exposure (rate of change of segregation). Using a mathematical approach and a series of checkboard shapes (Figure 14), the authors found that the intensity of segregation quantified by the CoV remained 1 for different mixing cases. However, the scale of segregation presented lower values as the mixing process was improving. Therefore, the authors concluded that the scale of segregation, which represents the thickness of striations in a fluid mixture could be considered the best indicator of mixing in various applications as opposed to the intensity of segregation. This scale tends to decrease exponentially when mixing is improved. Based on that, the CoV will not be considered, albeit calculated, as a mixing indicator in the present study.

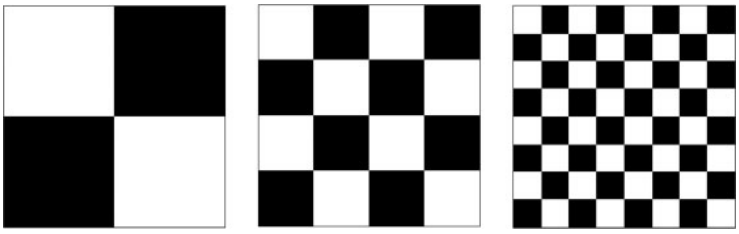

Figure 14: Checkerboard representation of a decreasing segregation scale with a constant CoV

1. Concentration Coefficient of Variance

The CoV is one description of the quality of mixing in a blending device. To calculate the CoV, the concentration of the fluid particles is evaluated at different positions across the channels. As such, the homogeneity of the mixture is quantified as follows:

$$CoV = \sqrt{\frac{1}{N_t}\sum_{j=1}^{N_t}\left(\frac{C_j - C_{mean}}{C_{mean}}\right)^2} \quad (14)$$

where, N_t = total number of material points at a cross-sectional area;

C_j = concentration at the ith material point;

C_{mean} = mean concentration at the slice;

Theoretically, a CoV with a value of 1 indicates pure segregation, while a value of 0 refers to pure homogeneity.

2. Segregation Scale

The segregation scale, introduced by Danckwerts (1952), is another parameter for mixing quantification. It represents the thickness of striations available at a fluid mixing surface. The thinning layers implicate a smaller segregation scale; thus, better mixing.

In the present work, the evaluation of the segregation scale is based on the correlogram method, which is the default method in Polyflow. Several authors also used this method to compute the scale of segregation, including Bothe et al. (Bothe et al., 2006) and Zhu et al. (Zhu et al. 2013) who used the same formulation proposed by Danckwerts to evaluate the length scale of segregation. Soman and Madhuranthakam evaluated distributive mixing in a similar fashion using the standard deviation of particles number to assess the distributive mixing inside several mixers (Soman and Madhuranthakam, 2017). Their method relies on the same approach used in the

correlogram method whereas a value of 100% standard deviation refers to complete segregation while lower values indicate higher distributive mixing.

The validity of the correlogram method requires that several conditions in the mixing field are met. These include the absence of long-range segregation and regular patterns in the mixture (Danckwerts, 1952). This is the case at hand as it can be seen from the observation of the concentration distribution at various locations that the particles are relocating at every time step from the injection point at the inlet. Moreover, the patterns are never repeated and the only form of large segregation is observed at the inlet. Therefore, the correlogram method was deemed appropriate for this case at hand.

The correlogram is a graphical description of temporal or spatial correlations between different sites, evaluated for a designated range of distances. For the current work, spatial correlations are used to measure the concentration similarity between pairs of material points with increasing distance. The geometry is sliced into surfaces using a displacement interval of one millimeter. *M* pairs of material points with varying distances, designated by *r*, are considered. Each point has an assigned concentration scalar, 0 or 1, depending on the imposed concentration profile. As the particles progress inside the channels, their locations are calculated and stored. The successive states of the concentration field are accordingly obtained. Then, the mean and standard deviation of concentration are calculated.

For a selected number of pairs of material points, the concentrations of an "i^{th}" pair are evaluated as $C_i^{'}$ and $C_i^{''}$. Then, the auto-correlation coefficient of concentration "*R*" is computed in function of the mean concentration and the variance.

$$R(r) = \frac{\sum_{i=1}^{M}(C_i{}' - C_{mean})(C_i{}'' - C_{mean})}{M\sigma^2} \tag{15}$$

At each slice of the mixer, the auto-correlation coefficient is evaluated and plotted against the increasing distance between material points. The resulting graph corresponds to the probability of finding a pair of material points with the same concentration separated by a distance *r* (Figure 15).

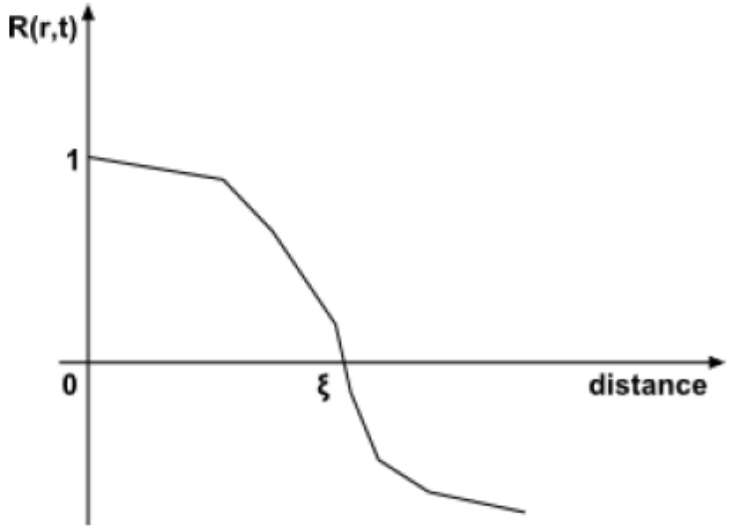

Figure 15: Autocorrelation function over a slice S

The integration of the auto-correlation coefficient in terms of distance defines the segregation scale *S*:

$$S = \int_0^{\xi} R(r)\, dr \tag{16}$$

Where ξ marks the point at which the auto-correlation coefficient R is null. This parameter is considered a measurement of the size of the regions with uniform concentration. It depends highly on the initial concentration profile and may be affected by the flow regime. In fact, the segregation scale offers a meaningful characterization of mixing especially in cases of lamellar structures where it designates the striations thickness.

CHAPTER IV

RESULTS AND DISCUSSION

A. Mesh Sensitivity Analysis

Numerical solutions require that the computational domain be carefully meshed in order to obtain accurate results. A coarse grid would therefore render results that cannot describe the smaller details of the flow, whereas a very fine mesh is computationally very costly. This renders tedious the completion of all tasks. For this reason, a mesh sensitivity analysis was undertaken in order to find the most suitable mesh that can be used to describe the flow. This was performed at the highest Reynolds number of 10. The technique followed the Grid Convergence Index (GCI) as a measure of convergence to the optimal grid size (Celik et al., 2008).

The Grid Convergence method is an approach for estimating the discretization error in a numerical simulation. It aims at predicting the dependence of a given variable on the grid resolution. For this reason, different grids are chosen based on their degree of refinement. The variable of interest is then calculated for each mesh until it becomes relatively independent of the grid size. This is translated into smaller errors between the obtained values quantified by the Grid Convergence Index.

In the present study, the various geometries were meshed separately using a structured hexahedral grid. Five mesh densities were considered starting with an element size of 1.5 mm down to 0.2 mm. GCI calculations were performed based on two parameters: pressure drop and scale of segregation. Both variables were calculated for each grid type and the relative errors were then computed. The results were

compared by sets of three: the coarse, the medium and the fine mesh. Acceptable GCI values are usually chosen to be less than 5% (Al Assaad et al., 2017). However, for a higher accuracy, the desired range of GCI values in the present study was set to be lower than 2%.

Convergence was obtained for an element size of 0.2 mm for all the geometries. The final values of the GCI for the optimal mesh are presented in Table 3. The corresponding number of elements for the full geometries is displayed, along with three other parameters: aspect ratio, skewness, and orthogonal quality of the given mesh. Those parameters are used to characterize the mesh quality. The aspect ratio measures stretching in cells, while skewness determines their similarity to ideal ones. As for the orthogonal quality, it quantifies the minimum intersection of grid lines at a 90˚ angle. For instance, the chosen mesh must satisfy the following conditions: The aspect ratio is smaller than 35, the skewness is smaller than 0.95, and the orthogonal quality is larger than 0.01 (ANSYS® Inc., 2019).

Table 3: GCI results and mesh quality for a 0.2 mm element size

Geometries	Gray	Chen	Double-SAR	Straight Duct
GCI (ΔP) %	0.74	1.98	0.95	0.26
GCI (segregation scale) %	1.37	0.87	0.41	0.005
Number of elements for full geometries	756,064	736,376	733,520	953,691
Aspect ratio	1.2753	1.3824	1.3294	3.1826

Skewness	0.08847	0.10516	0.09287	0.43126
Orthogonal quality	0.96341	0.95178	0.95998	0.68373

Table 3 also shows that the convergence indices for all the geometries were lower than 2%. The values of aspect ratio, skewness and orthogonal quality were also within the desired range as well. Therefore, a structured hexahedral mesh with 0.2 mm elements was chosen to model all the geometries.

B. Mixer Characterization

1. Pressure Drop

Pressure drop across the micromixers determines the pumping power required to move the fluid within the channels. Based on that, their energy consumption is estimated. Pressure losses between the inlet and the outlet of each mixer were evaluated for different Reynolds numbers. The results are illustrated in Figure 16.

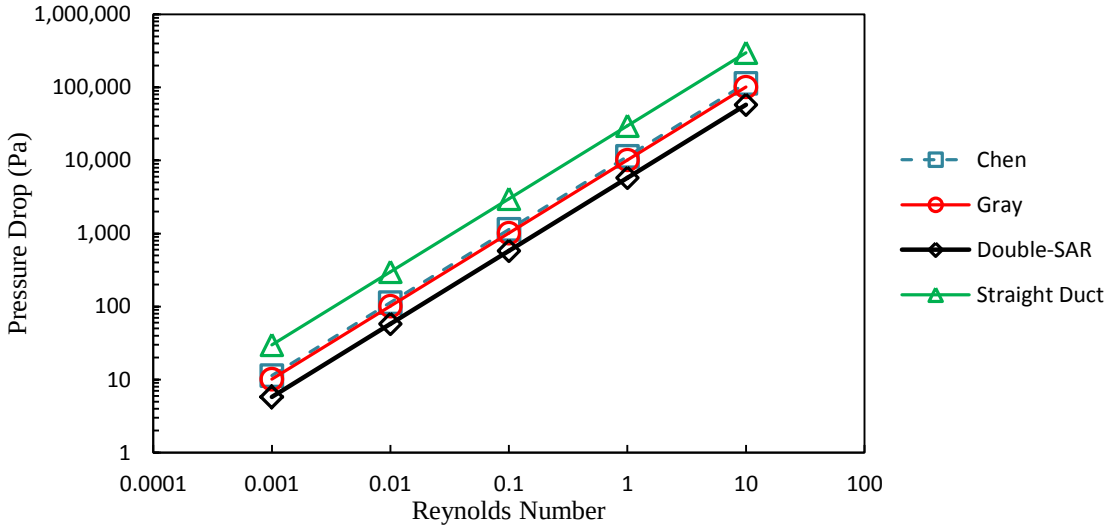

Figure 16: Pressure drop variation with Reynolds number for all the geometries

It can be seen that the pressure drop across the various micromixers increases as Re increases. This is expected since pressure drop is proportionally related to the velocity inside the channels.

To perform a more detailed comparison between the geometries, the pressure losses at Re = 0.001 are displayed in Figure 17.

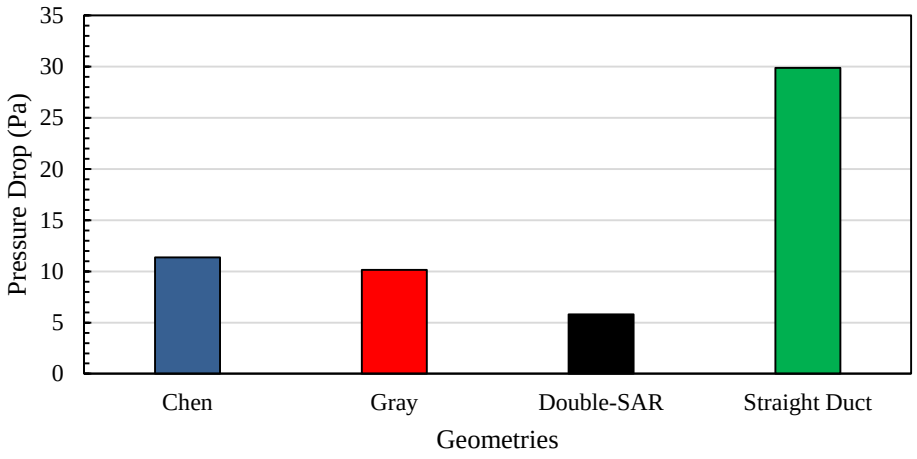

Figure 17: Pressure drop for all the geometries at Re = 0.001

The plot above shows that pressure drop is significantly lower in SAR geometries than a straight duct. For example, the losses in the straight channel are about 5-times higher than in Double-SAR. This is in line with findings in the literature which claims that the introduction of SAR patterns reduces Δp (Ghanem et al., 2013a). However, comparing the SAR geometries against each other shows that the Double SAR has the lowest pressure drop, followed by the mixer geometry of Gray then Chen.

The maximum pressure drop for the Double SAR (at Re = 10) was recorded at 57.904 kPa, while the geometries of Gray and Chen had values of 101.445 and 113.686 kPa respectively.

The reduced losses inside those geometries are affected by the splitting of the flowrate inside their channels. The separation action produces smaller velocities in the branches and thus reduces the pressure drop across the mixers.

Moreover, the velocity inside the geometries of Gray and Chen can reach lower values of $U_m/2$, as there is only one splitting point inside their mixing elements. However, for Double-SAR, it reaches $U_m/4$. Table 4 shows the volume fractions of the three SAR mixers where the velocity assumes values of U_m, $U_m/2$, or $U_m/4$. It is very clear that 46.1% of the Double SAR volume operates at much lower velocities, which explains its lower pressure drop requirement.

Table 4: Volume fractions of velocities across the Chen (9 units), Gray (12 units), and Double-SAR (4 units) geometries

	α (U_m)	β ($U_m/2$)	δ ($U_m/4$)
Chen	0.13	0.87	-
Gray	0.11	0.89	-
Double-SAR	0.039	0.5	0.461

Similar results were reported by Habchi et al. (2019), where the pressure losses for both Gray and Chen were evaluated using water as a working fluid at Re = 0.001.

Their findings were based on normalized values of pressure drop The authors proved that Gray is less energy consuming than Chen in terms of pressure losses.

Additionally, further comparison about pressure losses of the Gray and Chen geometries can be performed with the experimental results obtained by Anxionnaz et al. (2017). The authors evaluated the pressure losses for the geometries using the same glycerol-water solution (as in this study) for a Reynolds number span of 0.1 -3.3. Their results were converted to reflect pressure drop per mixing element in order to compare them to the current study. This comparison of *Δp per* mixing element for the Gray and Chen geometries against the experimental results of Anxionnaz et al. (2017) is presented in Figure 18.

It can be clearly seen that the mean relative error is 1.54% for the Gray geometry whereas it was calculated at 3.3% for the Chen geometry.

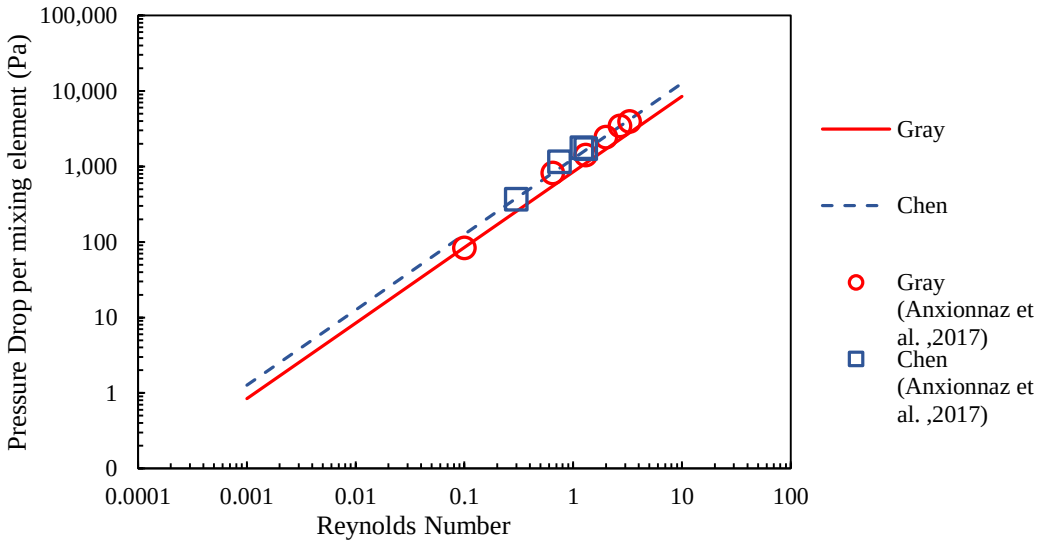

Figure 18: Comparison of Gray and Chen pressure drop per mixing element with literature values reported by Anxionnaz et al. (2017)

2. Fanning Friction Factor

The fanning friction factor is sometimes used as another measure of energy consumption. The evaluation of this parameter is needed to account for the friction losses inside the micromixers and to present an idea about the available shear stresses. The advantage of using this parameter is its sensitivity to variations in the velocity in the various sub-branches. The friction factor characterizes each geometry and takes into account the splitting of the flowrate. Furthermore, it represents the shear imposed by the fluid flow against the walls of the mixers considering the geometrical variations along the channels. Figure 19 shows the variation of the friction factor against the Reynolds number for all the geometries. It should be noted that the respective values of *f* were calculated using Equations (11), (13), and (14).

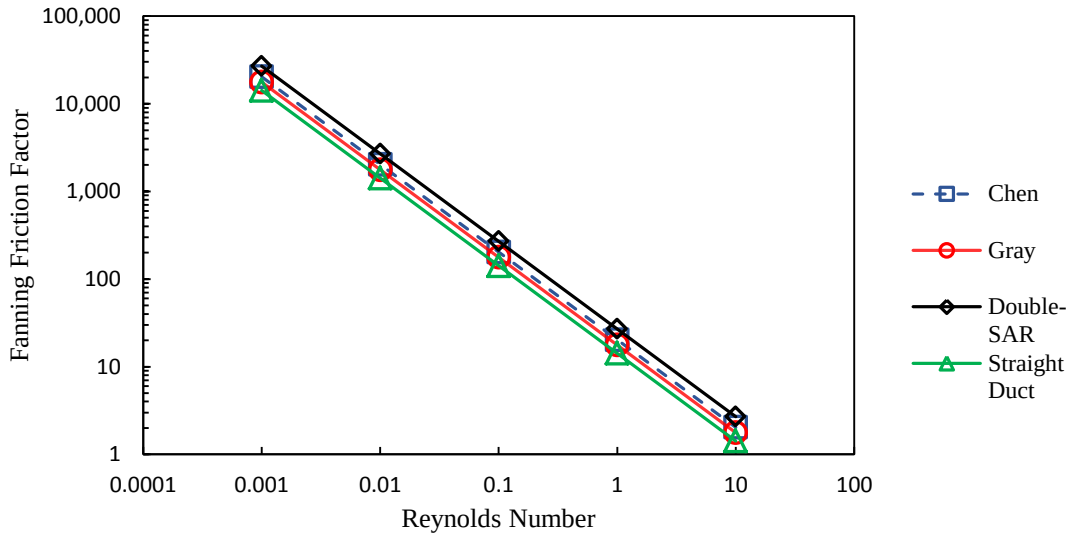

Figure 19: Fanning friction factor variation with Reynolds number

For creeping flows, an inversely proportional relationship between the friction factor and Re is expected. This is clearly obvious in Figure 4.

For a better assessment, the fanning friction factors of all the mixers were examined at Re = 0.1. The comparison of the coefficients, illustrated in Figure 20, reveals deeper findings related to shear stresses.

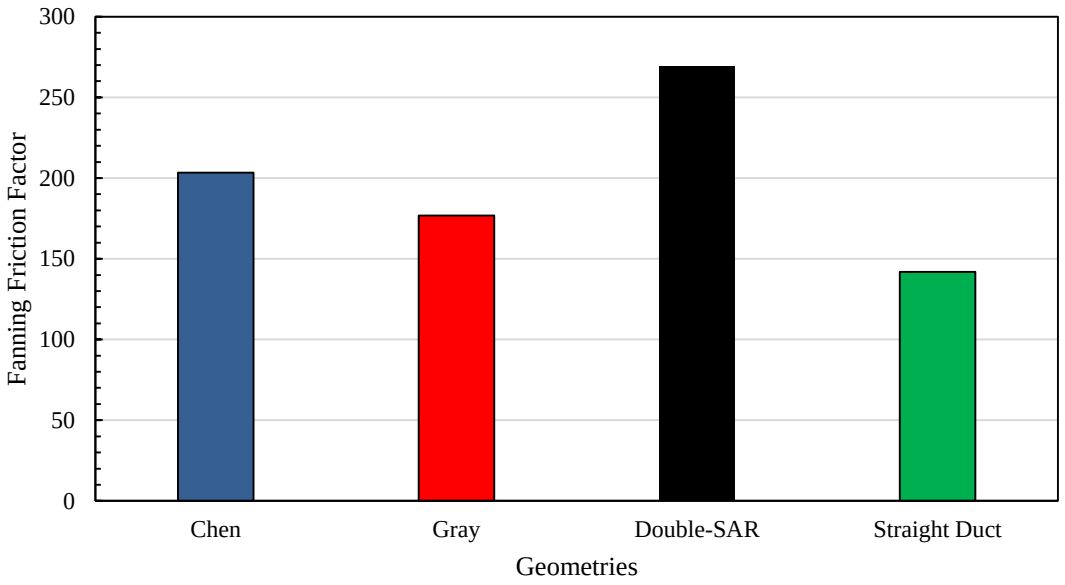

Figure 20: Fanning friction factor values for all the geometries at Re = 0.1

The friction losses inside the straight duct are the lowest with a coefficient of 141.9. In fact, the SAR geometries exhibit more friction caused by the occurrence of lower velocities and the presence of bends in their channels. The Double-SAR showed a

value that is 1.89-fold larger than a straight duct whereas those calculated for the geometries of Chen and Gray were 1.43-, and 1.24-fold larger, respectively.

While the other two SAR geometries have higher velocities, Gray presents more bends per unit than Chen. However, the latter presents more split-and-recombine patterns that produce additional friction losses.

3. Concentration Coefficient of Variance

To quantify the mixing efficiency of the mixers, two parameters were used in the current work, namely, the intensity of segregation (i.e. CoV) and the scale of segregation. First, the CoV was calculated for all Re at one millimeter displacements (on the straight length scale) inside the mixers. All simulations for the various geometries started with the same concentration profile as material points, with scalar concentrations of 0 and 1, were distributed evenly between two adjacent zones. Accordingly, the theoretical CoV at the inlet of all the mixers must be around 1, indicating full segregation.

The CoV variation across the four micromixers is illustrated in Figure 21 and Figure 22 at Re = 0.1 and Re = 1. These figures were also plotted using two distinct length scales of the geometry, namely, the straight length and the residence length.

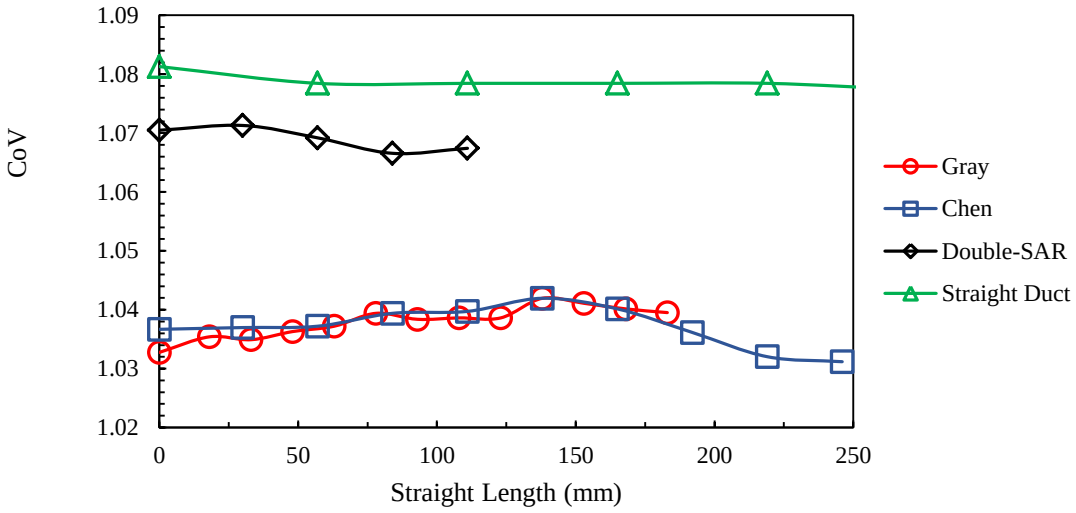

(a) CoV vs. straight length at Re = 0.1

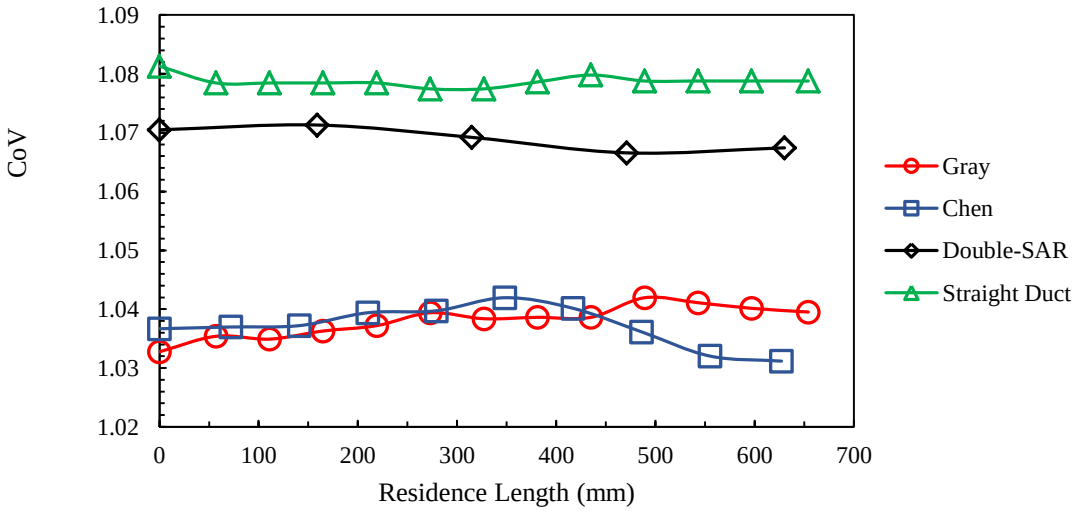

(b) CoV vs residence length at Re = 0.1

Figure 21: Variation of the CoV across the geometries at Re = 0.1 in terms of (a) straight length and (b) residence length

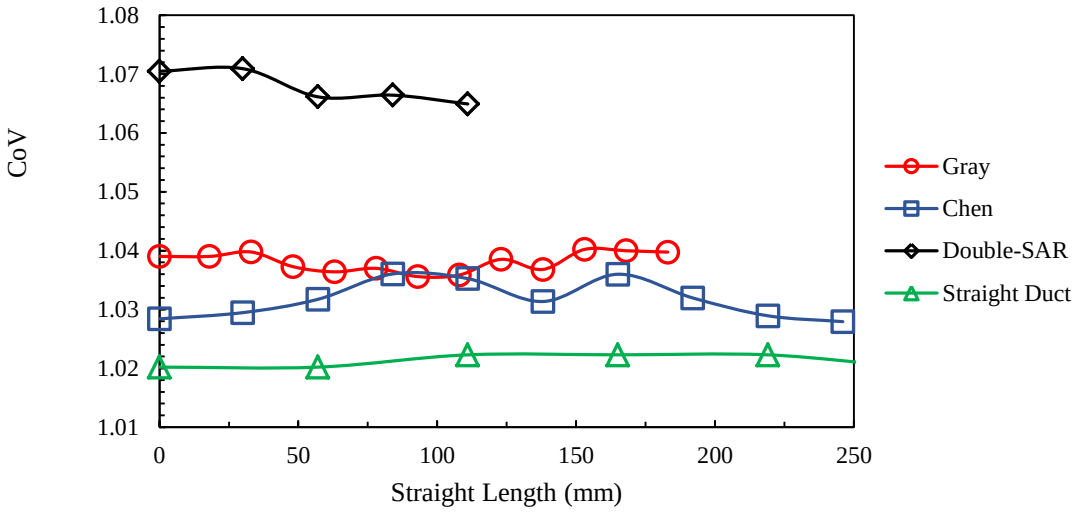

(a) CoV vs straight length at Re = 1

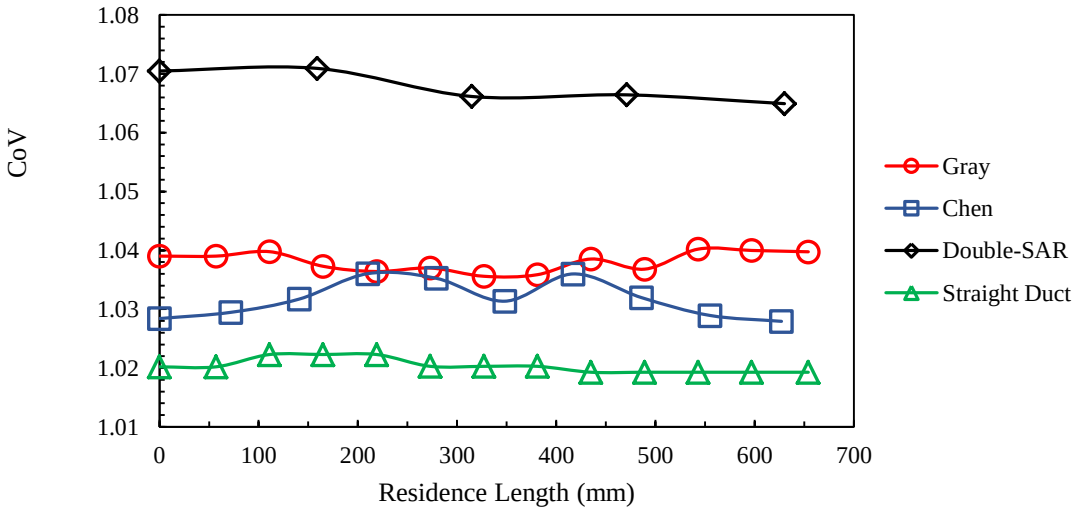

(b) CoV vs residence length at Re = 1

Figure 22: Variation of the CoV across the geometries at Re = 1 in terms of (a) straight length and (b) residence length.

It can be clearly seen that the CoV values at the inlet were almost 1 for all the geometries. This is expected as the material points with scalar concentrations of 0 and 1 are equally distributed at the beginning. However, as the flow progresses inside the

channels of the geometries, the CoV was found to remain constant and ranged between 1.02 and 1.08 even when the Reynolds number changed. The small deviation from the theoretical value of 1 can be attributed to the initial distribution of the particles since it is not an ideal one and therefore, few points of concentration scalar of 0 were mixed with those of a concentration scalar of 1. Nonetheless, the variation of the CoV across the SAR channels seems to be almost negligible. Even the increase in the Re number from 0.1 to 1 did not affect these values. This behavior was expected for the straight duct as no bends or mixing patterns exist, but not for the SAR geometries. However, it should be noted that the particles were being mixed and the concentration across the mixers was changing at each displacement (cf. Figure 24).

This behavior was however best explained by the work of Kukukova et al. (2009) who demonstrated that the CoV is highly dependent on the patterns obtained from the fluid particles. The authors demonstrated using a series of checkerboards that this mixing index may have a value of one even in the presence of a fully mixed state. Their numerical examples are shown in Figure 23 where a series of checkerboards identical to the mixing patterns obtained in the current study was used to demonstrate the variation of the CoV.

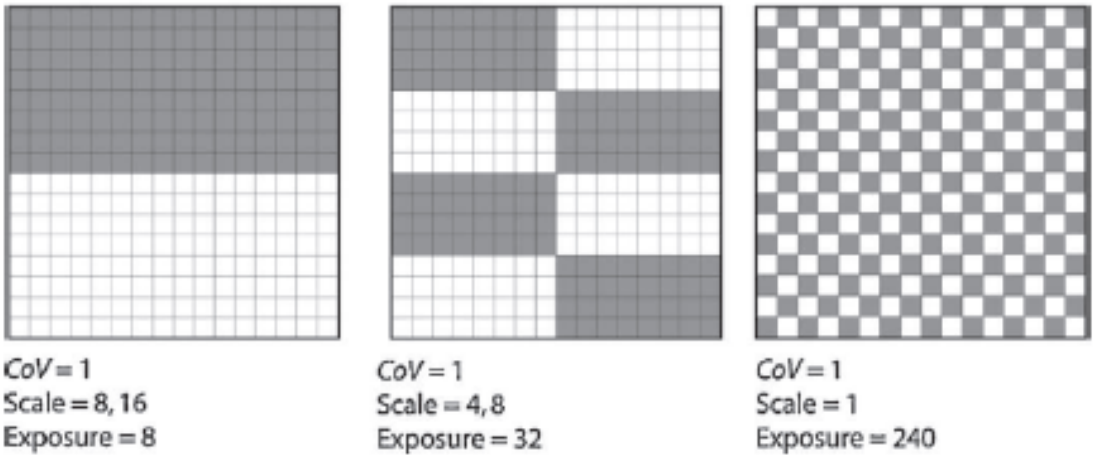

Figure 23: Checkerboard representations for the variation of three mixing indices: CoV, segregation scale, and exposure as reported by Kukukova et al. (2009)

For the same mean concentration, the white squares have a concentration of 0 while the black ones have a concentration of 1. The mixing increases from left to right. Accordingly, it would be expected that the intensity of segregation quantified by the CoV will decrease. However, it was shown that it remains constant.

This can be better explained by the definition of the intensity of segregation which states that this parameter quantifies the magnitude of variation of concentration but does not provide information concerning the arrangement of the scalar material points. Therefore, a constant CoV with a value around 1 was expected in the case of the SAR mixers as the same concentration profiles proposed by Kukukova et al. apply for the case of the SAR geometries. This can be observed in Figure 24 where the patterns of the fluid particles at the inlet, the middle, and the outlet of Double-SAR are shown.

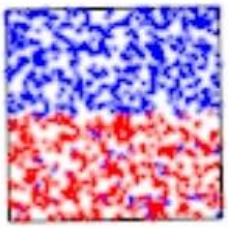
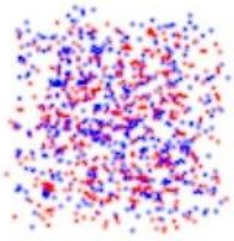
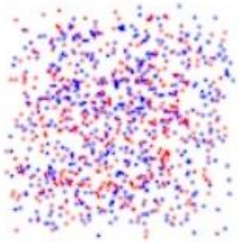

CoV = 1.070 CoV = 1.069 CoV = 1.067

Figure 24: Scalar mixing for Double-SAR at the inlet, the middle, and the outlet of the mixer

It can be clearly observed that the material points are being mixed, however the CoV value does not change.

To mitigate this problem and better quantify mixing, another parameter will be utilized, namely, the scale of segregation.

4. Scale of Segregation

The scale of segregation quantifies the mixing quality inside the channels. The thickness of the striations created after each split and recombine pattern is one indicator of the mixing quality. However, this length scale is not a measurement of the exact dimension of the clumps. In fact, it is a tool that describes the variability in concentration revealing the existence of both segregated and non-segregated patterns. It refers to a proportional average value of the whole concentration data field and supports sub-sampling when the assessment of a smaller structure in the mixing field is needed.

A qualitative assessment of the evolution of the scale of segregation inside the mixers is shown in Figure 25. The scalar mixing for the geometries is represented through illustrations of the concentration variation at various locations in the channels.

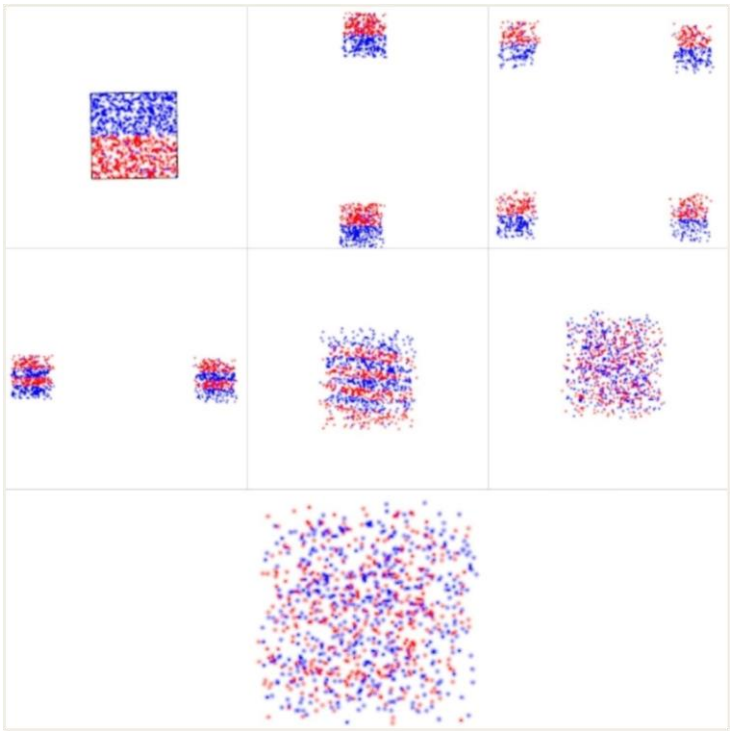

(a) Scalar mixing for Double-SAR at 0, 11, 18, 23, 28, 55, and 114 mm (from left to right)

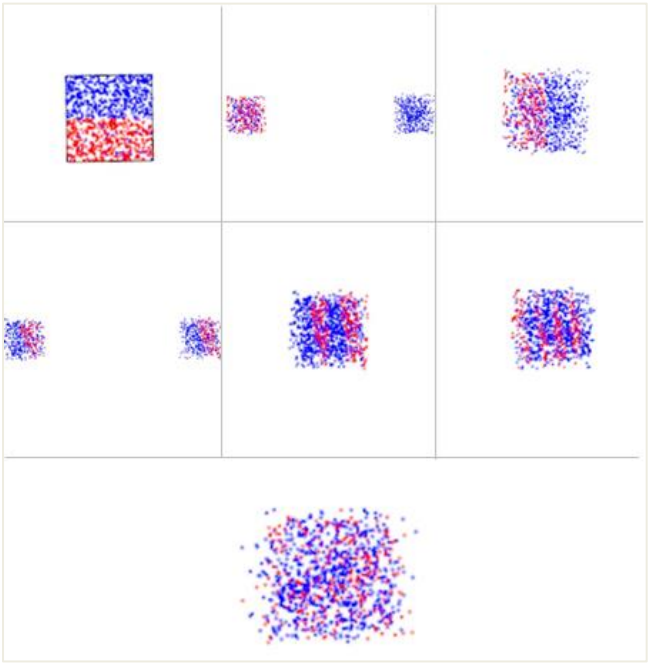

(b) Scalar mixing for Gray at 0, 10, 16, 25, 30, 45, and 186 mm (from left to right)

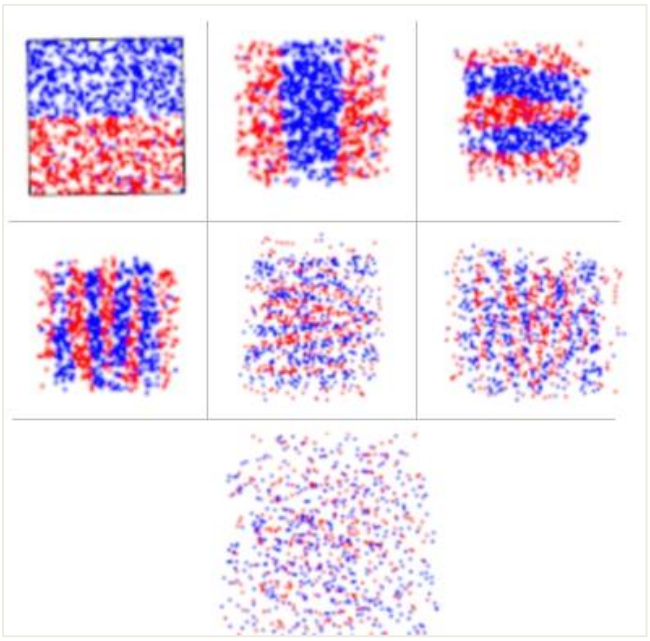

(c) Scalar mixing for Chen at 0, 16, 28, 44, 54, 71, and 249 mm (from left to right)

Figure 25:Concentration variation through scalar mixing for (a) Double-SAR, (b) Gray, (c) Chen

In the case of the SAR micromixers, there is a significant improvement in the mixing quality as the concentration gradient varies rapidly after the injection of the fluid particles.

The split-and-recombine mechanism produces more laminations with smaller thickness as the fluid flows inside the channels. It creates patterns similar to the theoretical model predicted by the Baker's transformation through stretching and folding of the fluid which further enhances the blending process.

Concerning the straight duct geometry, the concentration distribution remains almost the same for the whole conduit. Only slight changes in the concentration gradient

between the inlet and the outlet were observed at the interface between the particles, which was attributed to the presence of small numerical diffusion.

For a more quantitative evaluation, the variation of the scale of segregation relative to the various SAR geometries is plotted against that for the straight duct at Re = 1 in Figure 26. The variation of this length scale is presented along both the straight length and the residence length of the mixers.

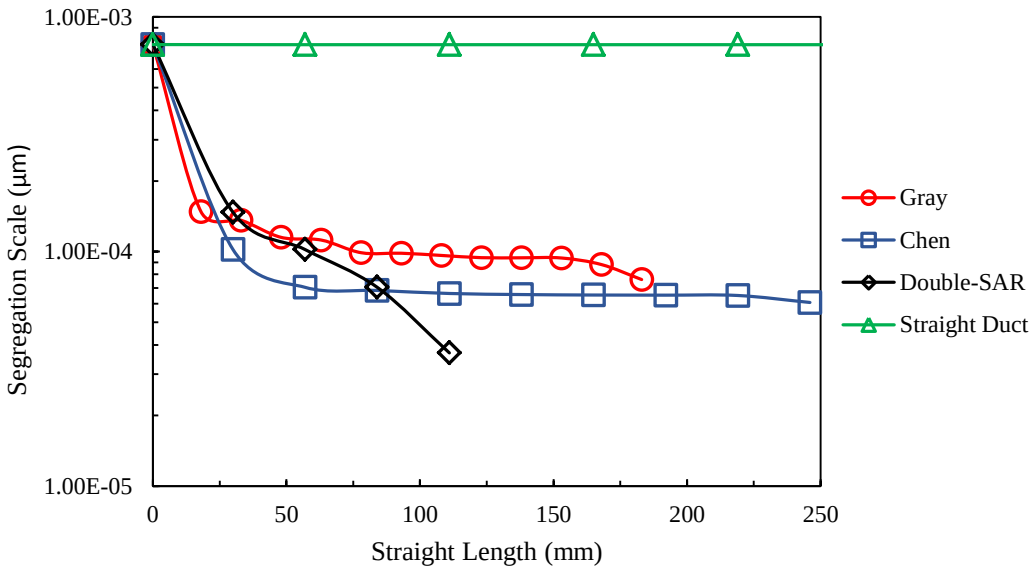

(a) Segregation scale vs. straight length

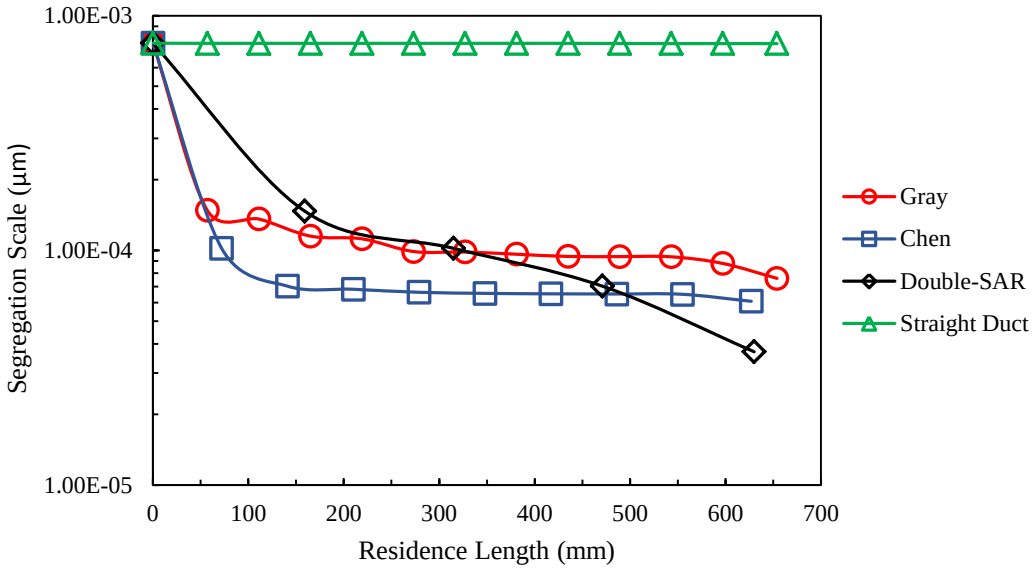

(b) Segregation scale vs. residence length

Figure 26: Variation of the scale of segregation across the mixers at Re = 1 in terms of (a) straight length and (b) residence length

The graphs clearly show the constant scale in the case of the straight duct due to the absence of any bends or mixing elements. The difference in segregation scales between the inlet and the outlet is negligible. However, a decreasing pattern is observed for Gray, Chen, and Double-SAR. Because all simulations started with the same inlet condition, the length scale has a common value of 762.9 µm at the inlet. This quickly decreases after the first mixing element until it steadies further downstream. As the fluid passes through the repetitive patterns of the Gray and Chen mixing elements, the scale starts decreasing at a slower rate. The same applies for the Double-SAR. However, the slope of the length scale remains steeper than those of Gray and Chen which reflects better mixing. In fact, the Double-SAR showed a superior mixing performance at

similar residence length but smaller straight length. This translates into a more compact design.

The split and recombine patterns create successive laminations of the fluids which enlarges the contact area between them. This process enhances blending by creating thin filaments of the fluids. Accordingly, the concentration distribution varies at each displacement away from the inlet as the clumps material points start shrinking and the segregation scale falls to very low values.

Moreover, the difference in the mixing quality for the complete range of Re numbers between the four geometries is presented in Figure 27, where the segregation scale at the outlet of each geometry is reported.

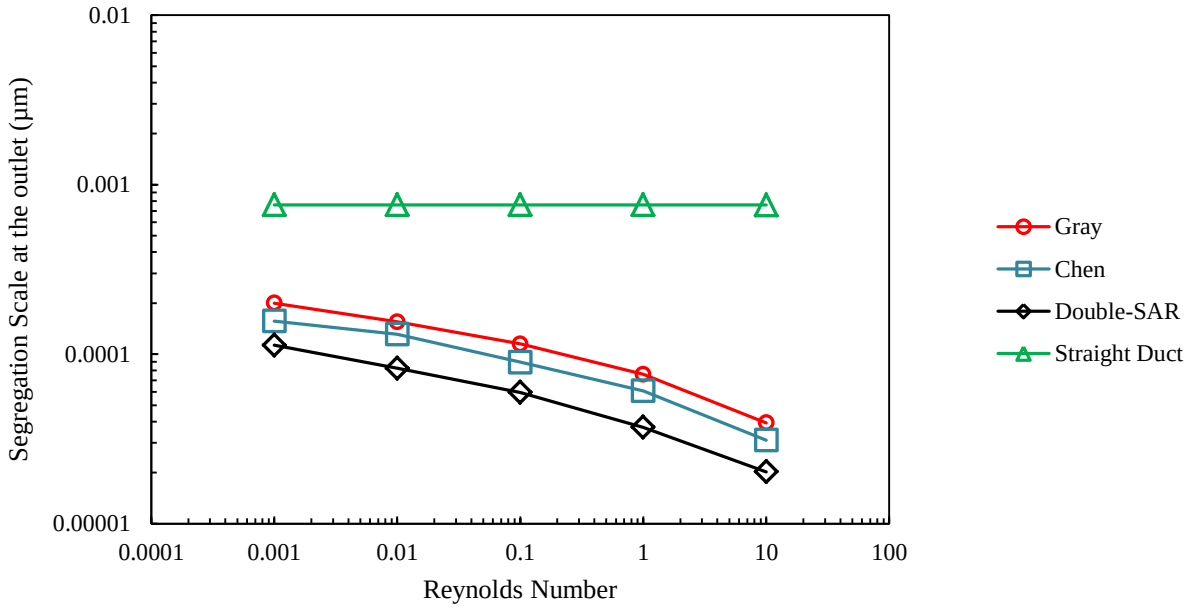

Figure 27: Variation of the scale of segregation at the outlet of the mixers with Reynolds number

The straight duct shows no mixing at all, which was expected. In the case of the SAR mixers, Figure 27 clearly shows the superior performance of the Double-SAR compared to the other geometries. Furthermore, the SAR design of Chen and Meiners (2004) shows a better mixing performance then Gray et al. (1999) for all Reynolds numbers.

Regarding Gray and Chen, the latter seems to offer lower length scales and better mixing efficiency. The results were in accord with the findings of Habchi et al., (2019) who reported better mixing in the Chen geometry compared to that of Gray et al..

Another observation is the effect of the Reynolds number on the scale of segregation. Effectively, smaller length scales are achieved at higher Re numbers; at Re = 10, the SAR geometries have 5-times greater scales than at Re = 0.001. This is also in line with the findings of Kukukova et al. (2011) who demonstrated that the length scales measured in a stirred tank reactor decrease with an increasing Re.

The examination of the proposed geometry against the others revealed interesting outcomes. On one hand, Double-SAR presents a superior performance in terms of mixing quality as it provides the smallest segregation scales at all Reynolds numbers. Chen is shown better than Gray as well with regards to mixing performance. On another hand, the new geometry seems to be less energy consuming than both Gray and Chen. In spite of having the lowest pressure drop, Double-SAR has the highest friction losses followed by Chen and Gray, considering the bends, the SAR patterns, and the reduced velocities.

CHAPTER V

CONCLUSIONS AND RECOMMENDATIONS

The performance of a novel geometry, the “Double SAR”, was numerically investigated for its mixing efficiency and energy consumption under creeping flow conditions. The design was assessed against previous geometries proposed by Chen and Meiners (Chen and Meiners, 2004) and Gray et al. (Gray et al., 1999) and a straight duct.

The pressure drop and friction factor relative to each geometry were examined to estimate the power requirements. Generally, pressure losses increased with an increase in Re. Moreover, it was found that Double SAR presents the lowest pressure drop amongst the mixers, followed by Gray, Chen, and the straight duct at last. This is

mainly attributed to the frequent occurrence of low velocities inside Double-SAR under the effect of a double split of the flowrate inside each mixing element compared to one split per element for Gray and Chen mixers. However, this was counter-balanced by a larger friction factor which indicates larger values of shear stresses inside the geometry. It was succeeded by Chen and Gray respectively, since the latter exhibits less split-and-recombine patterns per unit what reduces friction losses inside its channels.

Furthermore, two mixing indices, the CoV and the scale of segregation, were also evaluated in the present work to quantify the mixing efficiency of the designs. The CoV was shown to be independent of the Reynolds number. It remained constant with a value around 1 for all the mixers. On the contrary, the segregation scale decreased as mixing improved along the mixers. Smaller values were recorded at higher Reynolds numbers as well. The smallest length scale was achieved in the case of Double SAR marking the best mixing efficiency for the new geometry. The Chen mixer came next as it outperformed the Gray mixer in terms of mixing. The results obtained were in agreement with the findings of Kukukova et al. (Kukukova et al., 2009), Habchi et al. (2019) and Anxionnaz et al. (2017).

Based on the outcomes of the present work, it is possible to conclude that the Double SAR offers the best mixing quality among the SAR geometries at low energy cost with regard to pressure losses. In addition, for the same residence length, this geometry requires the least straight length, which makes it more compact than the others.

However, additional research can be performed to further explore the findings of the current work. As such, possible recommendations for future work may include:

- The use of an additional method for calculating the scale of segregation, namely, the PNN method which was proven to have highly accurate results in assessing the mixing quality in terms of this length scale.
- The evaluation of dispersive and distributive mixing inside the geometries using other mixing indices than the ones used in the present study.
- The use of experimental work as a support for the numerical computations using prototypes of the suggested designs for more realistic assessment.

APPENDIX I

MESH SENSITIVITY ANALYSIS

In the results below, pressure drop and mixing data obtained from the mesh sensitivity analysis simulations are presented. The GCI method is then introduced followed by GCI calculations performed for each geometry.

A. Pressure Drop Data

For the mesh study, one mixing unit of each geometry was considered. As such, average values of pressure were obtained at the inlet and the outlet of each mixing unit considering five mesh densities: coarse, intermediate, fine, finer, and finest.

Afterwards, the average pressure drop was evaluated as the difference between the average pressure at the inlet and the average pressure at the outlet. In the following tables, pressure values evaluated for each mesh density are presented.

5. Chen Geometry

Mesh type	Coarse	Intermediate	Fine	Finer	Finest
Average pressure at the inlet (Pa)	22,588.89	21,818.75	16,522.45	17,004.88	16,697.83
Average pressure at the outlet (Pa)	515.67	343.625	119.5633	83.80795	47
Pressure drop (Pa)	22,073.22	21,475.13	16,402.89	16,921.07	16,650.83

6. Gray geometry

Mesh type	Coarse	Intermediate	Fine	Finer	Finest
Average pressure at the inlet (Pa)	15,973.64	17,561.54	12,358.36	12,903.33	12,689.84
Average pressure at the outlet (Pa)	515.594	392.0207	119.916	74.841	46.971

7. Double geometry

Mesh type	Coarse	Intermediate	Fine	Finer	Finest
Average pressure at the inlet (Pa)	24,000.17	23,605	17,802.17	18,094.51	17,902.38
Average pressure at the outlet (Pa)	515.7209	345.3559	119.6374	81.8499	46.5387
Pressure drop (Pa)	23,484.45	23,259.64	17,682.53	18,012.66	17,855.84

8. Straight duct geometry

Mesh type	Coarse	Intermediate	Fine	Finer	Finest
Average pressure at the inlet (Pa)	109,529.3	90,355.62	77,742.24	76,641.68	76,138.17
Average pressure at the outlet (Pa)	509.59	281.258	119.6934	85.7877	46.2542
Pressure drop (Pa)	109,019.7	90,074.36	77,622.55	76,555.9	76,091.91

B. Mixing Data

In the following, the parameters extracted from tracing particles inside the mixers are presented. Four parameters were considered: the mean concentration $\bar{C}$, the standard deviation of concentration s concentration, the concentration coefficient of variance CoV, and the scale of segregation. For every geometry, data are recorded at the inlet and the outlet of one mixing unit.

9. Chen geometry

Mesh Type	Mixing Element	C_{mean}	$s_{concentration}$	CoV	Scale of segregation (m)
Coarse	0	0.449	0.497392	1.107777	7.648×10^{-4}
	1	0.3886364	0.4874404	1.254232	5.36×10^{-4}
Intermediate	0	0.471	0.499158	1.1059784	7.645×10^{-4}
	1	0.438478	0.4962	1.131641	5.319×10^{-4}
Fine	0	0.462	0.498553	1.07912	7.64×10^{-4}
	1	0.453524	0.497835	1.097704	5.203×10^{-4}
Finer	0	0.422	0.493878	1.170328	7.637×10^{-4}

	1	0.42026	0.4936	1.17451	5.13×10^{-4}
Finest	0	0.482	0.499675	1.036671	7.629×10^{-4}
	1	0.479919	0.499596	1.041	5.09×10^{-4}

10. Gray geometry

Mesh Type	Mixing element	C_{mean}	$s_{concentration}$	CoV	Scale of segregation (m)
Coarse	0	0.456244	0.47404	1.03901	7.644×10^{-4}
	1	0.456244	0.447405	1.03902	5.47×10^{-4}
Intermediate	0	0.414	0.43473	1.05007	7.658×10^{-4}
	1	0.4154	0.433318	1.043136	5.401×10^{-4}
Fine	0	0.418	0.431851	1.033138	7.639×10^{-4}
	1	0.4244	0.429601	1.012277	5.255×10^{-4}
Finer	0	0.451	0.474045	1.051098	7.633×10^{-4}

	1	0.45265	0.474045	1.047266	5.194×10^{-4}
Finest	0	0.391674	0.423372	1.080928	7.629×10^{-4}
	1	0.392082	0.4423813	1.080928	5.154×10^{-4}

11. Double geometry

Mesh Type	Mixing element	C_{mean}	$s_{concentration}$	CoV	Scale of segregation (m)
Coarse	0	0.475	0.499374	1.051315	7.909×10^{-4}
	1	0.474666	0.499357	1.052018	5.147×10^{-4}
Intermediate	0	0.448	0.497288	1.110019	7.769×10^{-4}
	1	0.453631	0.497845	1.097466	5.007×10^{-4}
Fine	0	0.452	0.49769	1.10108	7.634×10^{-4}
	1	0.452887	0.497775	1.099115	4.872×10^{-4}
Finer	0	0.455	0.49797	1.094441	7.622×10^{-4}
	1	0.4563	0.498086	1.091575	4.86×10^{-4}

Finest	0	0.46	0.498397	1.083472	7.629×10^{-4}
	1	0.46076	0.498458	1.081806	4.768×10-4

12. Straight duct geometry

Mesh Type	Straight length (mm)	C_{mean}	$s_{concentration}$	CoV	Scale of segregation (m)
Coarse	0	0.416	0.492893	1.18484	7.972×10^{-4}
	40	0.416416	0.492964	1.183825	7.967×10^{-4}
	80	0.416416	0.492964	1.183825	7.967×10^{-4}
	120	0.416416	0.492964	1.183825	7.967×10^{-4}
	161	0.416	0.492964	1.183825	7.7967×10^{-4}
Intermediate	0	0.468	0.498974	1.066185	7.865×10^{-4}
	40	0.467758	0.498959	1.066703	7.864×10^{-4}
	80	0.467758	0.498959	1.066703	7.864×10^{-4}
	120	0.467758	0.498959	1.066703	7.864×10^{-4}

	161	0.467	0.498959	1.066703	7.7864×10^{-4}
Fine	0	0.458	0.492794	1.07597	7.75×10^{-4}
	40	0.458	0.492794	1.07597	7.774×10^{-4}
	80	0.458	0.492794	1.07597	7.774×10^{-4}
	120	0.458	0.492794	1.07597	7.774×10^{-4}
	161	0.458	0.498232	1.087844	7.742×10^{-4}
Finer	0	0.464	0.498702	1.074789	7.64×10^{-4}
	40	0.464	0.498702	1.074789	7.634×10^{-4}
	80	0.464	0.498702	1.074789	7.634×10^{-4}
	120	0.464	0.498702	1.074789	7.634×10^{-4}
	161	0.464	0.498702	1.074789	7.7634×10^{-4}
Finest	0	0.455	0.496965	1.116777	7.629×10^{-4}
	40	0.455	0.496965	1.116777	7.625×10^{-4}

80	0.455	0.496965	1.116777	7.625×10^{-4}
120	0.455	0.496965	1.116777	7.625×10^{-4}
161	0.445	0.496965	1.116777	7.762×10^{-4}

C. GCI Calculations

As previously mentioned, the GCI calculations were based on the evaluation of two parameters: the scale of segregation and the pressure drop. In the following, the calculation method of the GCI is presented.

Three meshes with increasing densities designated by mesh 1, mesh 2, and mesh 3 are considered. For each mesh, the number of cells N and domain volume ΔV_i are extracted from the meshing software after choosing the desired element size. The relative grid size, h, is then calculated for each mesh as:

$$h = \left(\frac{1}{N}\sum_{i=0}^{N}\Delta V_i\right)^{1/3} \tag{17}$$

Next, the grid refinement ratio r defined for every pair of meshes is evaluated. This ratio must always be greater than 1.3 (Celik et al., 2008). In this case, r_{21} and r_{32}, are computed as:

$$r_{21} = \frac{h_2}{h_1} \tag{18}$$

$$r_{32} = \frac{h_3}{h_2} \tag{19}$$

The values of the variable tested for the independence study denoted by Φ_1, Φ_2, and Φ_3 are then introduced. The difference between two entries of the variable of interest is known as epsilon. This parameter is computed as well. Therefore, eps_{21} and eps_{32} are calculated:

$$eps_{21} = \Phi_2 - \Phi_1 \tag{20}$$

$$eps_{32} = \Phi_3 - \Phi_1 \tag{21}$$

Afterwards, the apparent order of the method p is calculated using the following set of equations:

$$p = \frac{1}{\ln(r_{21})} \left| ln \left| \frac{eps_{32}}{eps_{21}} \right| + q(p) \right| \tag{22}$$

$$q(p) = \left| ln \frac{{r_{21}}^p - s}{{r_{32}}^p - s} \right| \tag{23}$$

$$s = 1 \,.\, sign \left(\frac{eps_{32}}{eps_{21}} \right) \tag{24}$$

The system above is solved using a fixed-point iteration method. The extrapolated values of the chosen variable $\Phi_{ext\ 21}$ and $\Phi_{ext\ 32}$ are calculated as follows:

$$\Phi_{ext\ 21} = ({r_{21}}^{p}\ \Phi_1 - \Phi_2)/\ ({r_{21}}^{p} - 1) \tag{25}$$

$$\Phi_{ext\ 32} = ({r_{32}}^{p}\ \Phi_2 - \Phi_3)/\ ({r_{32}}^{p} - 1) \tag{26}$$

The final step is the evaluation of the relative error e_{32} along with the extrapolated error $e_{ext\ 32}$ from the following:

$$e_{\ 32} = \left|\frac{\Phi_2 - \Phi_3}{\Phi_2}\right| \tag{27}$$

$$e_{ext\ 32} = \left|\frac{\Phi_{ext\ 32} - \Phi_2}{\Phi_{ext\ 32}}\right| \tag{28}$$

The GCI is then computed as:

$$GCI = \frac{1.25\ e_{\ 32}}{{r_{32}}^{p} - 1} \tag{29}$$

Following this set of equations, the GCI was calculated for every set of three grids in terms of segregation scale and pressure drop. The values computed are presented in the tables below.

13. Chen Geometry

Table 5: GCI calculations for Chen geometry in terms of segregation scale

Mesh type	Coarse	Intermediate	Fine	Finer	Finest
Number of cells	200	675	5,400	23,414	87583
Domain volume (mm^3)	6.75×10^{-7}	6.75×10^{-7}	6.75×10^{-7}	6.75×10^{-7}	6.75×10^{-7}
Grid size (mm)	1.5	1	0.5	0.307	0.198
Ratio r		1.5	2	1.63	1.55
Scale of Segregation at the outlet (μm)	536.3	531.9	520.3	513	509
Eps		4.4	11.6	7.3	4
S			1		1
Q			0.6135		0.1540
Φ_{ext}		512.9	493.161	507.5	505.456
e (%)			2.23		0.79
e_{ext} (%)			5.5		0.7
P	1		2		

GCI (%)	6.52		0.87		

Table 6: GCI calculations for Chen geometry in terms of pressure drop

Mesh type	Coarse	Intermediate	Fine	Finer	Finest
Number of cells	200	675	5,400	23,414	87583
Domain volume (mm^3)	6.75×10^{-7}	6.75×10^{-7}	6.75×10^{-7}	6.75×10^{-7}	6.75×10^{-7}
Grid size (mm)	1.5	1	0.5	0.307	0.198
Ratio r		1.5	2	1.63	1.55
Pressure drop (Pa)	22,073.22	21,475.13	16,402.89	16,921.07	16,650.83
Eps		598.09	5072.24	-518.18	270.24
S			1		-1
Q			0.8485		0.0535
Φ_{ext}		20,943.9	14,474.45	17,357	16,386.6
e (%)			30.92		1.62
e_{ext} (%)			13.32		1.61
P	2		2		

GCI (%)	14.7	1.98

14. Gray geometry

Table 7: GCI calculations for Gray geometry in terms of segregation scale

Mesh type	Coarse	Intermediate	Fine	Finer	Finest
Number of cells	160	540	4,388	18,647	70,180
Domain volume (mm^3)	5.4×10^{-7}	5.4×10^{-7}	5.4×10^{-7}	5.4×10^{-7}	5.4×10^{-7}
Grid size (mm)	1.5	1	0.497	0.307	0.197
Ratio r		1.5	2.01	1.62	1.56
Scale of Segregation at the outlet (μm)	547	540.1	525.5	519.4	515.4
Eps		6.9	14.6	6.1	4
S			1		1
Q			0.58		0.1145
Φ_{ext}		473.4	446.447	511.7	509.767
e (%)			2.78		0.78

e_{ext} (%)		17.71	1.11
P	0	1	
GCI	18.8	1.37	

Table 8: GCI calculations for Gray geometry in terms of pressure drop

Mesh type	Coarse	Intermediate	Fine	Finer	Finest
Number of cells	160	540	4,388	18,647	70,180
Domain volume (mm^3)	5.4×10^{-7}	5.4×10^{-7}	5.4×10^{-7}	5.4×10^{-7}	5.4×10^{-7}
Grid size (mm)	1.5	1	0.497	0.307	0.197
Ratio r		1.5	2.01	1.62	1.56
Pressure drop (Pa)	15,458.0	17,169.521	12,238.4	12,828.4	12,642.
Eps		-1,711.4713	4,931.080	-590.05	185.62
S			-1		-1
Q			0.2288		0.0898
Φ_{ext}		19,936.4	8,421.445	13,032.1	12,567.9

e (%)		40.29	1.47
e_{ext} (%)		45.32	0.60
P	1	3	
GCI	38.99	0.74	

15. Double Geometry

Table 9: GCI calculations for Double geometry in terms of segregation scale

Mesh type	Coarse	Intermediate	Fine	Finer	Finest
Number of cells	432	1458	11,696	45,286	188,149
Domain volume (mm^3)	1.46×10^{-6}	1.46×10^{-6}	1.46×10^{-6}	1.46×10^{-6}	1.46×10^{-6}
Grid size (mm)	1.5	1	0.5	0.318	0.198
Ratio r		1.5	2	1.57	1.61
Scale of Segregation at the outlet (µm)	514.7	500.7	487.2	486	476.8
Eps		14	13.5	1.2	9.2
S			1		1

Q			0.7072		0.1125
Φ_{ext}		475.0	474.965	485.8	475.228
e (%)			2.77		1.93
e_{ext} (%)			2.58		0.33
P	1		4		
GCI (%)	3.14		0.41		

Table 10: GCI calculations for Double geometry in terms of pressure drop

Mesh type	Coarse	Intermediate	Fine	Finer	Finest
Number of cells	432	1458	11,696	45,286	188,149
Domain volume (mm^3)	1.46×10-6	1.46×10-6	1.46×10-6	1.46×10-6	1.46×10-6
Grid size (mm)	1.5	1	0.5	0.318	0.198
Ratio r		1.5	2	1.57	1.61
Pressure drop (Pa)	23,484.45	23,259.64	17,682.53	18,012.66	17,855.5
Eps		224.81	5,577.11	-330.13	157.12
S			1		-1

Q			1.0948		0.0258
Φ_{ext}		23,167.6	16,918.68	18,319.6	17,719.6
e (%)			31.54		0.88
e_{ext} (%)			4.51		0.77
P	3		2		
GCI (%)	5.4		0.95		

16. Straight duct geometry

Table 11: GCI calculations for straight duct geometry in terms of segregation scale

Mesh type	Coarse	Intermediate	Fine	Finer	Finest
Number of cells	432	1,449	11,592	37,454	187,536
Domain volume (mm^3)	1.45×10-6	1.45×10-6	1.45×10-6	1.45×10-6	1.45×10-6
Grid size (mm)	1.497	1	0.5	0.338	0.198
Ratio r		1.5	2	1.48	1.71
Pressure drop (Pa)	796.7	786.4	774.2	763.4	762.5
Eps		10.3	12.2	10.8	0.9

S			1		1
Q			0.6476		0.9986
Φ_{ext}		754.3	754.307	762.5	762.471
e (%)			1.58		0.12
e_{ext} (%)			2.64		3.74×10-3
P	1		6		
GCI (%)	3.21		4.67×10-3		

Table 12: GCI calculations for straight duct geometry in terms of pressure drop

Mesh type	Coarse	Intermediate	Fine	Finer	Finest
Number of cells	432	1,449	11,592	37,454	187,536
Domain volume (mm^3)	1.45×10^{-6}	1.45×10^{-6}	1.45×10^{-6}	1.45×10^{-6}	1.45×10^{-6}
Grid size (mm)	1.497	1	0.5	0.338	0.198
Ratio r		1.5	2	1.48	1.71
Pressure drop (Pa)	109,019.7	90,074.360	77,622.55	76,555.9	76,091.9
Eps		18,945.34	12,451.81	1,066.65	463.99

S			1		1
Q			0.8505		0.5400
Φ_{ext}		72,761.2	72,761.17	75,934.4	75,934.3
e (%)			16.04		0.61
e_{ext} (%)			6.68		0.21
P	2		3		
GCI (%)	7.83		0.26		

APPENDIX II

RAW DATA FROM THE SIMULATIONS OF FULL GEOMETRIES

In this section, pressure drop and mixing parameters extracted from the simulations of the full geometries are presented. The same approach used in the mesh sensitivity analysis was used to extract pressure drop and mixing data for the full geometries. The values were obtained at five Re numbers: 0.001, 0.01, 0.1, 1, and 10.

A. Pressure Drop Data

17. Chen geometry

Reynolds Number	0.001	0.01	0.1	1	10
Average pressure at the inlet (Pa)	11.37335	113.7335	1,137.335	11,373.35	113,733.5
Average pressure at the outlet (Pa)	0.004687	0.046867	0.468667	4.686672	46.86672
Pressure drop (Pa)	11.36867	113.6867	1,136.867	11,368.67	113,686.7

18. Gray geometry

Reynolds Number	0.001	0.01	0.1	1	10
Average pressure at the inlet (Pa)	10.14913	101.4926	1,014.913	10,149.13	101,491.3
Average pressure at the outlet (Pa)	0.004559	0.045592	0.455937	4.559367	45.59367
Pressure drop (Pa)	10.14457	101.447	1,014.457	10,144.57	101,445.7

19. Double geometry

Reynolds Number	0.001	0.01	0.1	1	10

Average pressure at the inlet (Pa)	5.795176	57.95176	579.5176	5,795.176	57,951.76
Average pressure at the outlet (Pa)	0.004699	0.04699	0.469895	4.698955	46.98955
Pressure drop (Pa)	5.790477	57.90477	579.0477	5,790.477	57,904.77

20. Straight duct geometry

Reynolds Number	0.001	0.01	0.1	1	10
Average pressure at the inlet (Pa)	29.88521	298.8521	2,988.521	29,885.21	298,553.3
Average pressure at the outlet (Pa)	0.006129	0.061292	0.382281	3.569109	35.63237
Pressure drop (Pa)	29.87908	298.7908	2,988.139	29,881.64	298,517.7

B. Mixing Data

21. Chen geometry

Re = 0.001

Mixing element	C_{mean}	$s_{concentration}$	CoV	Scale of segregation (m)
0	0.471	0.499158	1.059784	7.629×10^{-4}
1	0.467741	0.498958	1.066738	1.602×10^{-4}
2	0.465235	0.498789	1.072124	1.588×10^{-4}
3	0.459067	0.498321	1.085509	1.582×10^{-4}
4	0.461945	0.498549	1.079240	1.576×10^{-4}
5	0.462621	0.498600	1.077771	1.573×10^{-4}
6	0.463495	0.498665	1.075880	1.570×10^{-4}
7	0.460390	0.498428	1.082621	1.569×10^{-4}
8	0.457382	0.498180	1.089197	1.568×10^{-4}
9	0.451406	0.497633	1.102405	1.567×10^{-4}

Re = 0.01

Mixing element	C_{mean}	$s_{concentration}$	CoV	Scale of segregation (m)
0	0.464	0.498702	1.074789	7.629×10^{-4}
1	0.465235	0.498789	1.072124	1.631×10^{-4}
2	0.461851	0.498542	1.079443	1.59×10^{-4}
3	0.459876	0.498387	1.083742	1.436×10^{-4}
4	0.458592	0.498282	1.086548	1.395×10^{-4}

5	0.456932	0.498141	1.090186	1.354×10^{-4}
6	0.456008	0.498061	1.092218	1.346×10^{-4}
7	0.455240	0.497992	1.093911	1.324×10^{-4}
8	0.453837	0.497864	1.097010	1.313×10^{-4}
9	0.454035	0.497882	1.096571	1.312×10^{-4}

Re = 0.1

Mixing element	C_{mean}	$s_{concentration}$	CoV	Scale of segregation (m)
0	0.482	0.499675	1.036671	7.629×10^{-4}
1	0.481854	0.499670	1.036973	2.445×10^{-4}
2	0.481744	0.499666	1.037202	1.566×10^{-4}
3	0.480691	0.499627	1.039393	1.373×10^{-4}
4	0.480532	0.499620	1.039722	1.33×10^{-4}
5	0.479466	0.499578	1.041946	1.321×10^{-4}
6	0.480331	0.499613	1.040142	1.319×10^{-4}
7	0.482254	0.499685	1.036143	1.269×10^{-4}
8	0.484243	0.499751	1.032025	1.023×10^{-4}
9	0.484656	0.499764	1.031173	8.96×10^{-5}

Re = 1

Mixing element	C_{mean}	$s_{concentration}$	CoV	Scale of segregation (m)
0	0.486	0.499804	1.028403	7.629×10^{-4}
1	0.485485	0.499789	1.029462	1.016×10^{-4}
2	0.484390	0.499756	1.031721	7.10×10^{-5}
3	0.482305	0.499686	1.036038	6.83×10^{-5}
4	0.482688	0.499700	1.035243	6.63×10^{-5}
5	0.484567	0.499761	1.031355	6.56×10^{-5}
6	0.482325	0.499687	1.035990	6.53×10^{-5}
7	0.484276	0.499752	1.031956	6.52×10^{-5}
8	0.485744	0.499796	1.028929	6.50×10^{-5}
9	0.486228	0.499810	1.027932	6.07×10^{-5}

Re = 10

Mixing element	C_{mean}	$s_{concentration}$	CoV	Scale of segregation (m)
0	0.455	0.497970	1.094441	7.629×10^{-4}
1	0.455455	0.498011	1.093436	5.193×10^{-4}
2	0.452525	0.497741	1.099918	4.552×10^{-4}
3	0.452332	0.497722	1.100346	3.931×10^{-4}
4	0.451120	0.497605	1.103043	3.098×10^{-4}

5	0.452209	0.497710	1.100619	2.229×10^{-4}
6	0.451446	0.497636	1.102316	1.1603×10^{-4}
7	0.451813	0.497672	1.101500	1.151×10^{-4}
8	0.450365	0.497530	1.104725	9.16×10^{-5}
9	0.449685	0.497462	1.106244	3.11×10^{-5}

22. Gray Geometry

Re = 0.001

Mixing element	C_{mean}	$s_{concentration}$	CoV	Scale of segregation (m)
0	0.448247	0.468121	1.044337	7.629×10^{-4}
1	0.448056	0.467978	1.044463	3.231×10^{-4}
2	0.447519	0.467575	1.044816	2.57×10^{-4}
3	0.447125	0.467163	1.044816	1.984×10^{-4}
4	0.446436	0.466444	1.044816	1.989×10^{-4}
5	0.443706	0.464697	1.047309	1.982×10^{-4}
6	0.443401	0.464378	1.047309	1.98×10^{-4}
7	0.443701	0.464692	1.047309	1.984×10^{-4}
8	0.443029	0.463988	1.047309	1.98×10^{-4}
9	0.442381	0.463309	1.047309	1.987×10^{-4}
10	0.442373	0.463302	1.047309	1.992×10^{-4}
11	0.437856	0.459923	1.050396	1.974×10^{-4}

12	0.435779	0.457741	1.050396	1.947×10^{-4}

Re = 0.01

Mixing element	C_{mean}	$s_{concentration}$	CoV	Scale of segregation (m)
0	0.442954	0.464515	1.048677	7.629×10^{-4}
1	0.442671	0.464219	1.048677	2.674×10^{-4}
2	0.442332	0.463791	1.048514	1.819×10^{-4}
3	0.441474	0.462892	1.048514	1.793×10^{-4}
4	0.443153	0.462938	1.044646	1.72×10^{-4}
5	0.442597	0.462357	1.044646	1.675×10^{-4}
6	0.442694	0.462459	1.044646	1.618×10^{-4}
7	0.442360	0.463061	1.046796	1.603×10^{-4}
8	0.441738	0.462411	1.046796	1.602×10^{-4}
9	0.441938	0.462619	1.046796	1.598×10^{-4}
10	0.442039	0.462725	1.046796	1.591×10^{-4}
11	0.442270	0.462967	1.046796	1.563×10^{-4}
12	0.442895	0.463621	1.046796	1.55×10^{-4}

Re = 0.1

Mixing element	C_{mean}	$s_{concentration}$	CoV	Scale of segregation (m)
0	0.362	0.480578	1.032756	7.629×10^{-4}
1	0.361083	0.480314	1.035395	3.867×10^{-4}
2	0.361251	0.480363	1.034911	2.013×10^{-4}
3	0.360772	0.480224	1.036292	1.892×10^{-4}
4	0.361224	0.480355	1.034988	1.759×10^{-4}
5	0.362051	0.480593	1.032609	1.742×10^{-4}
6	0.361944	0.480562	1.032917	1.729×10^{-4}
7	0.359749	0.479926	1.039248	1.722×10^{-4}
8	0.360673	0.480195	1.036579	1.676×10^{-4}
9	0.359325	0.479802	1.040477	1.612×10^{-4}
10	0.359028	0.479715	1.041339	1.454×10^{-4}
11	0.360255	0.480074	1.03778	1.363×10^{-4}
12	0.3596585	0.4799003	1.039512	1.15×10^{-4}

Re = 1

Mixing element	C_{mean}	$s_{concentration}$	CoV	Scale of segregation (m)
0	0.486	0.499804	1.028403	7.629×10^{-4}
1	0.485485	0.499789	1.029462	1.016×10^{-4}

2	0.484390	0.499756	1.031721	7.1×10^{-5}
3	0.482305	0.499686	1.036038	6.83×10^{-5}
4	0.482688	0.499700	1.035243	6.63×10^{-5}
5	0.484567	0.499761	1.031355	6.56×10^{-5}
6	0.482328	0.499687	1.035990	6.53×10^{-5}
7	0.484276	0.499752	1.031956	6.52×10^{-5}
8	0.485744	0.499796	1.028929	6.5×10^{-5}
9	0.486228	0.499810	1.027932	6.07×10^{-5}

Re = 10

Mixing element	C_{mean}	$s_{concentration}$	CoV	Scale of segregation (m)
0	0.391674	0.423372	1.080928	7.629×10^{-4}
1	0.392082	0.423813	1.080928	5.666×10^{-4}
2	0.391957	0.423479	1.080420	4.811×10^{-4}
3	0.391883	0.423398	1.080420	4.203×10^{-4}
4	0.391568	0.423059	1.080420	3.784×10^{-4}
5	0.3918456	0.423358	1.080420	3.242×10^{-4}
6	0.3908249	0.422673	1.081489	2.921×10^{-4}
7	0.390043	0.421827	1.081489	2.161×10^{-4}
8	0.389391	0.421122	1.081489	1.369×10^{-4}

9	0.389531	0.42127	1.08148	7.05×10^{-5}
10	0.389202	0.420918	1.081489	5.17×10^{-5}
11	0.389484	0.421223	1.081489	4.14×10^{-5}
12	0.389153	0.420865	1.081489	3.93×10^{-5}

23. Double Geometry

Re = 0.001

Mixing element	C_{mean}	$s_{concentration}$	CoV	Scale of segregation (m)
0	0.476	0.499423	1.049209	7.629×10^{-4}
1	0.478128	0.499521	1.044743	1.432×10^{-4}
2	0.477200	0.499479	1.046687	1.1329×10^{-4}
3	0.471251	0.499172	1.059249	1.1294×10^{-4}
4	0.459770	0.498378	1.083974	1.1128×10^{-4}

Re = 0.01

Mixing element	C_{mean}	$s_{concentration}$	CoV	Scale of segregation (m)
0	0.444	0.496854	1.119040	7.629×10^{-4}
1	0.440968	0.496503	1.12593	1.68×10^{-4}

2	0.441025	0.496509	1.125807	1.549×10^{-4}
3	0.441207	0.496531	1.125393	1.31×10^{-4}
4	0.440713	0.496472	1.126520	8.25×10^{-5}

Re = 0.1

Mixing element	C_{mean}	$s_{concentration}$	CoV	Scale of segregation (m)
0	0.466	0.498842	1.070477	7.629×10^{-4}
1	0.466331	0.498865	1.069764	1.453×10^{-4}
2	0.466599	0.498883	1.069189	1.004×10^{-4}
3	0.467824	0.498963	1.066562	9.34×10^{-5}
4	0.467425	0.498937	1.067417	5.95×10^{-5}

Re = 1

Mixing element	C_{mean}	$s_{concentration}$	CoV	Scale of segregation (m)
0	0.466	0.498842	1.070477	7.629×10^{-4}
1	0.465794	0.498828	1.070919	1.465×10^{-4}
2	0.468020	0.498976	1.066142	1.015×10^{-4}
3	0.467889	0.498967	1.066421	9.45×10^{-5}

4	0.468589	0.499012	1.064925	3.7×10^{-5}

Re = 10

Mixing element	C_{mean}	$s_{concentration}$	CoV	Scale of segregation (m)
0	0.448	0.497288	1.110019	7.629×10^{-4}
1	0.448241	0.497313	1.109478	4.908×10^{-4}
2	0.448731	0.497364	1.108380	3.004×10^{-4}
3	0.448416	0.497332	1.109084	1.804×10^{-4}
4	0.447776	0.497265	1.110520	2.02×10^{-5}

24. Straight duct geometry

Re = 0.001

Straight length (mm)	C_{mean}	$s_{concentration}$	CoV	Scale of segregation (m)
0	0.488	0.499856	1.024295	7.629×10^{-4}
57	0.487927	0.499854	1.024443	7.62×10^{-4}
111	0.486868	0.499827	1.026616	7.618×10^{-4}
165	0.484264	0.499752	1.031983	7.618×10^{-4}
219	0.484631	0.499763	1.031224	7.618×10^{-4}

273	0.487526	0.499844	1.025267	7.618×10^{-4}
327	0.490986	0.499918	1.018193	7.61×10^{-4}
381	0.484815	0.499769	1.030844	7.61×10^{-4}
435	0.488839	0.499875	1.022576	7.61×10^{-4}
489	0.489631	0.499892	1.020956	7.61×10^{-4}
543	0.498786	0.499998	1.002430	7.60×10^{-4}
597	0.505025	0.499974	0.989999	7.60×10^{-4}
654	0.501997	0.499996	0.996013	7.60×10^{-4}

Re = 0.01

Straight length (mm)	C_{mean}	$s_{concentration}$	CoV	Scale of segregation (m)
0	0.45	0.497493	1.105541	7.629×10^{-4}
57	0.450803	0.497573	1.103749	7.623×10^{-4}
111	0.450802	0.497573	1.103749	7.623×10^{-4}
165	0.450251	0.497518	1.104980	7.623×10^{-4}
219	0.451158	0.497608	1.102958	7.623×10^{-4}
273	0.451158	0.497608	1.102958	7.612×10^{-4}
327	0.451158	0.497608	1.102958	7.612×10^{-4}
381	0.451158	0.497608	1.102958	7.612×10^{-4}
435	0.451158	0.497608	1.102958	7.612×10^{-4}
489	0.451158	0.497608	1.102958	7.612×10^{-4}

543	0.451158	0.497608	1.102958	7.6015×10^{-4}
597	0.451158	0.497608	1.102958	7.6015×10^{-4}
654	0.451158	0.497608	1.102958	7.6015×10^{-4}

Re = 0.1

Straight length (mm)	C_{mean}	$s_{concentration}$	CoV	Scale of segregation (m)
0	0.461	0.498476	1.081294	7.629×10^{-4}
57	0.462311	0.498577	1.078444	7.621×10^{-4}
111	0.462311	0.498577	1.078444	7.621×10^{-4}
165	0.462311	0.498577	1.078444	7.621×10^{-4}
219	0.462311	0.498577	1.078444	7.611×10^{-4}
273	0.462311	0.498577	1.078444	7.611×10^{-4}
327	0.462776	0.498612	1.077436	7.611×10^{-4}
381	0.462776	0.498612	1.077436	7.611×10^{-4}
435	0.461693	0.498530	1.079786	7.611×10^{-4}
489	0.462159	0.498566	1.078774	7.759×10^{-4}
543	0.462159	0.498566	1.078774	7.759×10^{-4}
597	0.462159	0.498566	1.078774	7.759×10^{-4}
654	0.462159	0.498566	1.078774	7.759×10^{-4}

Re = 1

Straight length (mm)	C_{mean}	$s_{concentration}$	CoV	Scale of segregation (m)
0	0.49	0.4999	1.020204	7.629×10^{-4}
57	0.49	0.4999	1.020204	7.624×10^{-4}
111	0.48897	0.499878	1.022292	7.624×10^{-4}
165	0.48897	0.499878	1.022292	7.624×10^{-4}
219	0.48897	0.499878	1.022292	7.624×10^{-4}
273	0.489959	0.499899	1.020286	7.616×10^{-4}
327	0.489959	0.499899	1.020286	7.616×10^{-4}
381	0.489959	0.499899	1.020286	7.616×10^{-4}
435	0.490452	0.499908	1.019281	7.616×10^{-4}
489	0.490452	0.499908	1.019281	7.616×10^{-4}
543	0.490452	0.499908	1.019281	7.597×10^{-4}
597	0.490452	0.499908	1.019281	7.597×10^{-4}
654	0.490452	0.499908	1.019281	7.597×10^{-4}

Re = 10

Straight length (mm)	C_{mean}	$s_{concentration}$	CoV	Scale of segregation (m)
0	0.482	0.499675	1.036671	7.629×10^{-4}
57	0.479919	0.499596	1.041000	7.7625×10^{-4}

111	0.479919	0.499596	1.041000	7.7625×10^{-4}
165	0.479919	0.499596	1.041000	7.7625×10^{-4}
219	0.479919	0.499596	1.041000	7.7611×10^{-4}
273	0.479919	0.499596	1.041000	7.7611×10^{-4}
327	0.479919	0.499596	1.041000	7.7611×10^{-4}
381	0.479919	0.499596	1.041000	7.7611×10^{-4}
435	0.479919	0.499596	1.041000	7.7603×10^{-4}
489	0.479919	0.499596	1.041000	7.7603×10^{-4}
543	0.479919	0.499596	1.041000	7.7594×10^{-4}
597	0.479919	0.499596	1.041000	7.7594×10^{-4}
654	0.479919	0.499596	1.041000	7.7594×10^{-4}

APPENDIX III

SAMPLE CALCULATION

A. Fanning Friction Factor

The Fanning friction factor was calculated using Equations (11), (13), and (14)for the straight duct, Chen and Gray geometries, and Double geometry. In the following, a sample calculation of the friction factor relative to the Chen geometry at Re = 1 is presented. For this geometry and Re number, the following conditions are used:

Table 13: Physical parameters for the calculation of the Chen fanning friction factor

Re	1
Pressure drop (Pa)	11,368.66
Hydraulic diameter (m)	3.00×10^{-3}
Residence length (m)	6.54×10^{-1}
Density (kg/m3)	1,015
Velocity (m/s)	6.89×10^{-2}
Velocity/2 (m/s)	3.45×10^{-2}
Alpha	3/23
Beta	20/23

The fanning friction factor equation corresponding to the Chen geometry is:

$$f = \alpha \frac{\Delta p \, D_h}{2L\rho {U_m}^2} + \beta \frac{\Delta \, D_h}{2L\rho (\frac{U_m}{2})^2} \tag{30}$$

Accordingly, f is calculated as:

$$f = 0.87 \frac{11{,}368.66 \times 0.003}{2 \times 0.627 \times 1{,}015 \times 0.0689^2} + 0.13 \frac{11{,}368.66 \times 0.003}{2 \times 0.627 \times 1{,}015 \times 0.0345^2} \tag{31}$$

$$f = 2.033 \tag{32}$$

Following the same procedure, the fanning friction factor for every geometry is evaluated based on the proper equation and conditions. In the table below, the results for the friction factor calculations are reported:

Table 14: Fanning friction factor results for all the geometries at various Re numbers

Reynolds Number	Chen	Gray	Double	Straight duct
0.001	20330.76	17672.12201	26910.89	14195.50655
0.01	20330.76	1767.234856	2691.089	1419.550658
0.1	2033.076	176.7212198	269.1089	141.9660237
1	203.3076	17.67212197	26.91089	14.1967229
10	20.33076	1.767212201	2.691089	1.418253047

As another confirmation of the accuracy of the current results, the theoretical fanning friction factor for a straight channel, which is given by Equation (12), was used to validate the computations. The estimated values for a straight duct were therefore plotted against the theoretical ones in Figure 28.

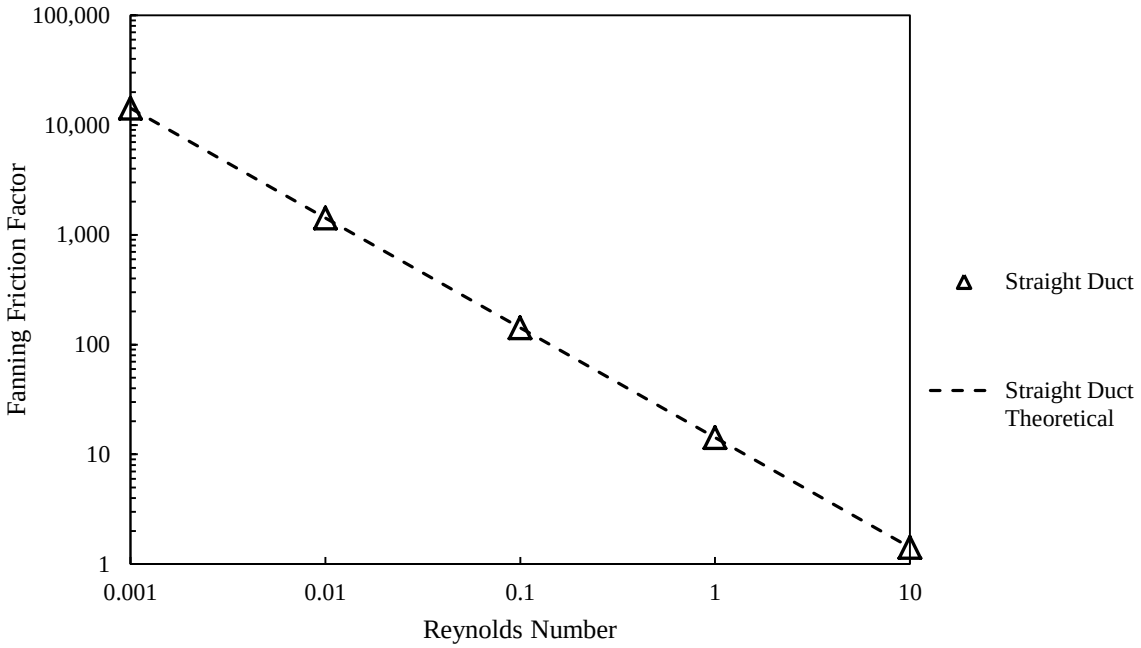

Figure 28: Comparison of theoretical and numerical values of the Fanning friction factor for a straight duct

It can be clearly discerned that negligible variation exists between the two approaches with the maximum error being present at the highest Re value of 10. At this condition, the relative error was found to be 0.313%.

BIBLIOGRAPHY

Ansari, M. A., & Kim, K. (2010). Mixing performance of unbalanced split and recombine micromixers with circular and rhombic sub-channels. Chemical Engineering Journal,162(2), 760-767.

ANSYS, Inc. (2019). Academic Research Mechanical, Release 19.0, Help System: ANSYS Polyflow User's Guide. Canonsburg, PA: ANSYS, Inc.

Anxionnaz-Minvielle, Z., Tochon, P., Couturier, R., Magallon, C., Théron, F., Cabassud, M., & Gourdon, C. (2017). Implementation of 'chaotic' advection for viscous fluids in heat exchanger/reactors. Chemical Engineering and Processing: Process Intensification,113, 118-127.

Assaad, D. A., Ghali, K., Ghaddar, N., & Habchi, C. (2017). Mixing ventilation coupled with personalized sinusoidal ventilation: Optimal frequency and flow rate for acceptable air quality. Energy and Buildings,154, 569-580.

Aubin, J., Fletcher, D., Bertrand, J., & Xuereb, C. (2003). Characterization of the Mixing Quality in Micromixers. Chemical Engineering & Technology,26(12), 1262-1270.

Bothe, D., Stemich, C., & Warnecke, H. (2006). Fluid mixing in a T-shaped micro-mixer. Chemical Engineering Science,61(9), 2950-2958.

Carrière, P. (2007). On a three-dimensional implementation of the baker's transformation. Physics of Fluids,19(11), 118110.

Celik, I.B., Ghia, U., Roache, P.J., Freitas, C.J., Coleman, H., Raad, P.E., 2008. Procedure for Estimation and Reporting of Uncertainty Due to Discretization in CFD Applications. Journal of Fluids Engineering,130, 078001–078004.

Chen, H., & Meiners, J. (2004). Topologic mixing on a microfluidic chip. Applied Physics Letters,84(12), 2193-2195.

Chen, J. J., Lai, Y. R., Tsai, R. T., Lin, J. D., & Wu, C. Y. (2011a). Crosswise ridge micromixers with split and recombination helical flows. Chemical Engineering Science,66(10), 2164-2176.

Chen, J. J., Chen, C. H., & Shie, S. R. (2011b). Optimal Designs of Staggered Dean Vortex Micromixers. International Journal of Molecular Sciences,12(6), 3500-3524.

Chorin, A. J. (1997). A Numerical Method for Solving Incompressible Viscous Flow Problems. Journal of Computational Physics,135(2), 118-125.

Danckwerts, P. V. (1952). The definition and measurement of some characteristics of mixtures. Applied Scientific Research,3(4), 279-296.

Donea, J., & Huerta, A. (2003). Finite Element Methods for Flow Problems.

Ghanem, A., Lemenand, T., Valle, D. D., & Peerhossaini, H. (2013a). Transport Phenomena in Passively Manipulated Chaotic Flows: Split-and-Recombine Reactors. Volume 1B, Symposia: Fluid Machinery; Fluid Power; Fluid-Structure Interaction and Flow-Induced Noise in Industrial Applications; Flow Applications in Aerospace; Flow Manipulation and Active Control: Theory, Experiments and Implementation; Fundamental Issues and Perspectives in Fluid Mechanics.

Ghanem, A., Lemenand, T., Valle, D. D., & Peerhossaini, H. (2013b). Optimized Chaotic Heat Exchanger Configurations for Process Industry: A Numerical Study. Volume 1B, Symposia: Fluid Machinery; Fluid Power; Fluid-Structure Interaction and Flow-Induced Noise in Industrial Applications; Flow Applications

in Aerospace; Flow Manipulation and Active Control: Theory, Experiments and Implementation; Fundamental Issues and Perspectives in Fluid Mechanics.

Ghanem, A., Lemenand, T., Valle, D. D., & Peerhossaini, H. (2014). Static mixers: Mechanisms, applications, and characterization methods – A review. Chemical Engineering Research and Design, 92(2), 205-228.

Gray, B., Jaeggi, D., Mourlas, N., Drieënhuizen, B. V., Williams, K., Maluf, N., & Kovacs, G. (1999). Novel interconnection technologies for integrated microfluidic systems. Sensors and Actuators A: Physical,77(1), 57-65.

Habchi, C., Lemenand, T., & Azizi, F. (2018). Mixing Enhancement in a Novel Type of "Split and Recombine" Static Mixer. Volume 7: Fluids Engineering.

Habchi, C., Ghanem, A., Lemenand, T., Valle, D. D., & Peerhossaini, H. (2019). Mixing performance in Split-And-Recombine Milli-Static Mixers—A numerical analysis. Chemical Engineering Research and Design,142, 298-306.

Heniche, M., & Tanguy, P. A. (2008). Finite Element Modeling of Viscous Mixing: A Review. Chemical Product and Process Modeling,3(1).

Hossain, S., & Kim, K. (2015). Mixing analysis in a three-dimensional serpentine split-and-recombine micromixer. Chemical Engineering Research and Design,100, 95-103.

Jarrahi, M., Thermeau, J., & Peerhossaini, H. (2016). Heat Transfer Enhancement in Split and Recombine Flow Configurations: A Numerical and Experimental Study. Volume 1: Heat Transfer in Energy Systems; Thermophysical Properties; Theory and Fundamentals in Heat Transfer; Nanoscale Thermal Transport; Heat

Transfer in Equipment; Heat Transfer in Fire and Combustion; Transport Processes in Fuel Cells and Heat Pipes; Boiling and Condensation in Macro, Micro and Nanosystems.

Kukukova, A., Aubin, J., & Kresta, S. M. (2009). A new definition of mixing and segregation: Three dimensions of a key process variable. Chemical Engineering Research and Design,87(4), 633-647.

Kukukova, A., Aubin, J., & Kresta, S. M. (2011). Measuring the scale of segregation in mixing data. The Canadian Journal of Chemical Engineering, 89(5), 1122-1138.

Langtangen, H. P., Mardal, K., & Winther, R. (2002). Numerical methods for incompressible viscous flow. Advances in Water Resources,25(8-12), 1125-1146.

Lee, S. W., Kim, D. S., Lee, S. S., & Kwon, T. H. (2006). A split and recombination micromixer fabricated in a PDMS three-dimensional structure. Journal of Micromechanics and Microengineering,16(5), 1067-1072.

Marques, M. P., & Fernandes, P. (2011). Microfluidic Devices: Useful Tools for Bioprocess Intensification. Molecules,16(10), 8368-8401.

Moukalled, F. H., Mangani, L., & Darwish, M. S. (2016). The finite volume method in computational fluid dynamics: An advanced introduction with OpenFOAM® and Matlab®. Cham: Springer.

Neerincx, P. E., Denteneer, R. P., Peelen, S., & Meijer, H. E. (2011). Compact Mixing Using Multiple Splitting, Stretching, and Recombining Flows. Macromolecular Materials and Engineering,296(3-4), 349-361.

Ohkawa, K., Nakamoto, T., Izuka, Y., Hirata, Y., & Inoue, Y. (2008). Flow and mixing characteristics of σ-type plate static mixer with splitting and inverse recombination. Chemical Engineering Research and Design,86(12), 1447-1453.

Parsa, M. K., & Hormozi, F. (2014). Experimental and CFD modeling of fluid mixing in sinusoidal microchannels with different phase shift between side walls. Journal of Micromechanics and Microengineering,24(6), 065018.

Schönfeld, F., Hessel, V., & Hofmann, C. (2004). An optimised split-and-recombine micro-mixer with uniform 'chaotic' mixing. Lab Chip,4(1), 65-69.

Soman, S. S., & Madhuranthakam, C. M. (2017). Effects of internal geometry modifications on the dispersive and distributive mixing in static mixers. Chemical Engineering and Processing: Process Intensification,122, 31-43.

Thakur, R., Vial, C., Nigam, K., Nauman, E., & Djelveh, G. (2003). Static Mixers in the Process Industries—A Review. Chemical Engineering Research and Design,81(7), 787-826.

Viktorov, V., Mahmud, M. R., & Visconte, C. (2016). Numerical study of fluid mixing at different inlet flow-rate ratios in Tear-drop and Chain micromixers compared to a new H-C passive micromixer. Engineering Applications of Computational Fluid Mechanics,10(1), 182-192.

Wiggins, S., & Ottino, J. M. (2004). Foundations of chaotic mixing. Philosophical Transactions of the Royal Society A: Mathematical, Physical and Engineering Sciences, 362(1818), 937-970.

Zhu, X. Z., Wang, G., He, Y. D., & Cheng, Z. F. (2013). Study of Dynamic Flow and Mixing Performances of Tri-Screw Extruders with Finite Element Method. Advances in Mechanical Engineering,5, 236389.